

OPTICAL FUNCTIONALIZATION OF CRYOLITE POLYCRYSTALS USING  
TRANSITION METAL/RARE EARTH IONS FOR THE APPLICATION OF  
LIGHTING AND BIOLOGICAL IMAGING

by

YUANSHU ZHOU

A thesis submitted to the

School of Graduate Studies

Rutgers, The State University of New Jersey

In partial fulfillment of the requirements

For the degree of

Master of Science

Graduate Program in Chemical and Biochemical Engineering

Written under the direction of

Richard E. Riman

And approved by

---

---

---

New Brunswick, New Jersey

January, 2018

## ABSTRACT OF THESIS

Optical Functionalization of Cryolite polycrystals using Transition metal/Rare earth

ions for the Applications of lighting and biological imaging

By YUANSHU ZHOU

Thesis Director:

Richard E. Riman

Cryolite ( $\text{Na}_3\text{AlF}_6$ ) was assumed to be a promising luminescent host for near-infrared photon emission with transition metal (TM)/rare earth (RE) ions as dopants. Micron cryolite samples were obtained through hydrothermal reaction, while nanocrystals were synthesized via solvothermal reaction. It is demonstrated that  $\text{RE}^{3+}$  ions having large radii cannot be doped into  $\text{Na}_3\text{AlF}_6$  host lattice by replacing  $\text{Al}^{3+}$  sites that with smaller radius. TM ions ( $\text{TM}=\text{Mn}^{2+}$ ,  $\text{Ni}^{2+}$ ,  $\text{Cr}^{3+}$ ,  $\text{Fe}^{3+}$ ) are successfully doped into  $\text{Na}_3\text{AlF}_6$  with substitution of  $\text{Al}^{3+}$  sites, while the  $\text{Cr}^{3+}$  doped  $\text{Na}_3\text{AlF}_6$  exhibited broad efficient deep-red emission at  $\sim 720$  nm. A systematic study of luminescence intensity versus  $\text{Cr}^{3+}$  concentration was explored to obtain the optimized cryolite phosphor. Energy decay dynamics was systematically analyzed on the basis of

theoretical model and experimental data. Heat-treated micron phosphor and  $\text{Na}_3\text{AlF}_6:60\text{mol}\%\text{Cr}^{3+}@\text{Na}_3\text{AlF}_6$  nanoparticles were proved to have efficient luminescence, which create big chance for advanced red/far-red light-emitting diodes (LEDs) and specific application like bioimaging in vivo.

## Acknowledgements

Foremost, I would like to thank my thesis advisor Prof. Richard E. Riman of the Department of Materials Science and Engineering at Rutgers, The State University of New Jersey, for his patience, motivation, enthusiasm, and immense knowledge. His guidance helped me in all the time of research and writing of this thesis, and consistently allowed this paper to be my own work.

Besides my advisor, I would like to thank another important Post-doctoral Fellow Dechao Yu involved in this research project, for his encouragement, insightful comments, and hard questions. He gave me so much guidance on experiments and data analysis, the research could not have been successfully conducted without his passionate participation and input.

Finally, I must express my very profound gratitude to my parents Xiaohui Zhou and Yuhuai Li, for giving birth to me and supporting me spiritually throughout my life. Also, I have to thank all my friends for providing me with unfailing support and continuous encouragement throughout my years of study and life. This accomplishment would not have been possible without them.

## Table of Contents

Abstract of thesis.....	ii
Acknowledgements.....	iv
List of Tables .....	vi
List of Figures .....	vii
1. Introduction.....	1
2. Experimental Methods .....	6
2.1. Chemicals .....	6
2.2. Hydrothermal synthesis .....	7
2.3. Solvothermal synthesis .....	9
2.4. Post-heat treatment on hydrothermal $\text{Na}_3\text{AlF}_6\text{:Cr}^{3+}$ phosphors .....	11
2.5. Becke line measurement.....	12
2.6. Characterization.....	12
3. Results and discussion .....	15
3.1. Phase identification .....	15
3.1.1. Hydrothermal Crystallization.....	15
3.1.2. Solvothermal Crystallization .....	16
3.1.3. Rare Earth doping .....	16
3.1.4. Transition metal doping .....	18
3.2. Refractive index value determined by Becke line measurement .....	22
3.3. Optical diffuse reflectance spectrum.....	24
3.4. Photoluminescence properties .....	25
4. Conclusions.....	34
Appendix.....	54
References.....	55

## List of Tables

Table 1. The measured refractive index value of the cryolite/chiolite solid solution mixture synthesized by different fluorine sources .....	35
Table 2. Rise time $t_{\text{rise}}$ of decay curve, fitting function, R-squared ( $R^2$ ), fitting parameter, and calculated decay time as a function of $\text{Cr}^{3+}$ concentration in $\text{Na}_3\text{AlF}_6$ under pulsed light excitation of 420 nm. ....	36

## List of Figures

Figure 1 Crystal structures of a typical monoclinic $\text{Na}_3\text{AlF}_6$ cryolite crystal.....	37
Figure 2 (a) Scheme of facile hydrothermal reaction to synthesize cryolite polycrystals. (b) Optical photograph of Teflon-lined stainless steel autoclave .....	38
Figure 3 The diagram of solvothermal reaction setup .....	39
Figure 4 The measured XRD patterns of as-synthesized cryolite powders using $\text{NH}_4\text{F}$ fluoride source and different ratios of $\text{Na}^+ : \text{Al}^{3+}$ in the raw materials .....	40
Figure 5 The measured XRD patterns of as-obtained cryolite powders using $\text{HF}$ fluoride source and varying $\text{Na}^+ : \text{Al}^{3+}$ ratios in the raw materials .....	41
Figure 6 The measured XRD patterns of as-synthesized cryolite nanocrystals at 240, 280 and 320°C, and that of cryolite standard. The image insets show the dispersion of the corresponding cryolite nanocrystals dispersed in DI water .....	42
Figure 7 The XRD patterns of the $\text{RE}^{3+}$ -doped cryolite ( $\text{RE}=\text{Er}, \text{Eu}, \text{Pr}$ ) products.....	43
Figure 8 SEM images of $\text{RE}^{3+}$ -doped cryolite polycrystals synthesized through hydrothermal reaction: (a) $\text{Na}_3\text{AlF}_6$ : 1mol% $\text{Er}^{3+}$ , (b) $\text{Na}_3\text{AlF}_6$ : 10mol% $\text{Er}^{3+}$ , (c) $\text{Na}_3\text{AlF}_6$ : 1mol% $\text{Pr}^{3+}$ , (d) $\text{Na}_3\text{AlF}_6$ : 10mol% $\text{Pr}^{3+}$ , (e) $\text{Na}_3\text{AlF}_6$ : 1mol% $\text{Eu}^{3+}$ , and (f) $\text{Na}_3\text{AlF}_6$ : 10mol% $\text{Eu}^{3+}$ .....	44
Figure 9 (a) The XRD patterns of hydrothermal synthesized $\text{Na}_3\text{AlF}_6$ :2mol% $\text{Ni}^{2+}$ , $\text{Na}_3\text{AlF}_6$ :2mol% $\text{Mn}^{2+}$ , and $\text{Na}_3\text{AlF}_6$ :2mol% $\text{Fe}^{3+}$ , and (b) that of $\text{Na}_3\text{AlF}_6$ doped with various $\text{Cr}^{3+}$ concentration .....	45
Figure 10 (a) SEM micrograph and (b) EDX spectra analysis of $\text{Na}_3\text{AlF}_6$ :60mol% $\text{Cr}^{3+}$ synthesized via hydrothermal reaction. (c) SEM micrographs and (d) EDX spectra analysis of the corresponding $\text{Na}_3\text{AlF}_6$ :60mol% $\text{Cr}^{3+}$ phosphors heat-treated at 700°C for 36 h.....	46
Figure 11 (a) Bright-field and (b) dark-field TEM images and (c) the corresponding SAED patterns of as-synthesized $\text{Na}_3\text{AlF}_6$ :60mol% $\text{Cr}^{3+}$ nanocrystals, respectively. .	47
Figure 12 (a) Diffuse reflectance spectrum of $\text{Na}_3\text{AlF}_6$ : $\text{Cr}^{3+}$ phosphor. (b) The as-obtained $\text{Na}_3\text{AlF}_6$ : $\text{Cr}^{3+}$ suspension after hydrothermal reaction. (c) The corresponding dry $\text{Na}_3\text{AlF}_6$ : $\text{Cr}^{3+}$ products after washing .....	48
Figure 13 (a) Excitation spectrum of $\text{Na}_3\text{AlF}_6$ : $\text{Cr}^{3+}$ phosphors monitored at about 720 nm. (b) Emission spectra (solid curves) of $\text{Na}_3\text{AlF}_6$ : $\text{Cr}^{3+}$ under 420 and 580 nm excitation.....	49

Figure 14 The $\text{Cr}^{3+}$ concentration-dependent emission spectrum of $\text{Na}_3\text{AlF}_6:\text{Cr}^{3+}$ phosphors under excitation of 420 nm. Normalized emission intensity in the inset of Figure 14 shows emission peak shift versus $\text{Cr}^{3+}$ concentration. ....	50
Figure 15 Fluorescence decay curves of $\text{Cr}^{3+}: {}^4\text{T}_2(4\text{F}) \rightarrow {}^4\text{A}_2 \sim 720 \text{ nm}$ as a function of $\text{Cr}^{3+}$ concentration in $\text{Na}_3\text{AlF}_6$ under pulsed light excitation of 420 nm. The inset shows the buildup in the first 150 $\mu\text{s}$ of the curves.....	51
Figure 16 (a) Comparative emission spectra and (b) decay curves of the $\text{Na}_3\text{AlF}_6: 60\text{mol}\%\text{Cr}^{3+}$ sample before (green dot curve) and after (red dot curve) heat treatment, respectively .....	52
Figure 17 (a) Luminescence spectra and (b) decay curves of $\text{Na}_3\text{AlF}_6: 60\text{mol}\%\text{Cr}^{3+}$ micron phosphors (red triangle line), $\text{Na}_3\text{AlF}_6: 60\text{mol}\%\text{Cr}^{3+}$ nanocrystals (blue dot line) and $\text{Na}_3\text{AlF}_6: 60\text{mol}\%\text{Cr}^{3+}@\text{Na}_3\text{AlF}_6$ nanocrystals (green square line) under excitation of 420 nm, respectively .....	53



## 1. Introduction

Cryolite, a mineral belonging to the aluminum fluoride group, shows great commercial value due to their industrial importance in melting process for years.<sup>1</sup> However, there is less research to explore its possibility as luminescent host. Interestingly, cryolite has refractive index ( $n$ ) of 1.3385, rather close to  $n \sim 1.3325$  of water.<sup>2</sup> As light travels through biological tissues, the absorption tends to attenuate due to the light scattering caused by cellular components *in vivo*.<sup>3</sup> Most tumors exhibit a wide array of refractive indices ranging from 1.33 to 1.48.<sup>4</sup> It is possible to use cryolite as optical probes significantly reducing the light scattering losses. Moreover, cryolite as fluoride has low phonon energy approximately  $500 \text{ cm}^{-1}$ , which makes it be a promising efficient luminescent host especially for near-infrared photon emission if optical functionalization was achieved by doping rare earth (RE)/transition metal (TM) activator ions. Meanwhile, the high melting point  $\sim 1000^\circ\text{C}$  of the cryolite crystals enable phosphor to feature good thermal stability as it works in an encapsulated light-emitting diodes (LEDs).<sup>5</sup>

Up to now, lots of nanomaterials such as quantum dots and single-walled carbon nanotubes have been proved dominantly for bioimaging application.<sup>6,7</sup> On the other

hand, the most recent popular research reveals that, using 808 and 980 nm laser excitation,  $\text{RE}^{3+}$  singly doped and  $\text{RE}^{3+}/\text{Yb}^{3+}$  co-doped  $\text{NaYF}_4$  nanocrystals (NCs) exhibit efficient visible up-conversion and/or near-infrared (NIR) down-conversion for molecular imaging and tissue imaging *in vivo*.<sup>8</sup> Especially, the excitation and emission of NIR down-conversion system are both located in the first ( $\sim 600\text{-}950$  nm) and/or second ( $\sim 1000\text{-}1700$  nm) NIR biologically transparent window, which would enable deep penetration and high-resolution bioimaging *in vivo* by greatly reducing light scattering losses. Besides, the TM dopants like  $\text{Cr}^{3+}$  were proposed for its interesting luminescent properties. For instance,  $\text{Cr}^{3+}$ -doped YAG:  $\text{Ce}^{3+}$  phosphors yield very strong deep-red emission peak at 690 nm,<sup>9</sup> and the  $\text{AB}_2\text{O}_4:\text{Cr}^{3+}$  ( $\text{A}=\text{Zn, Mg, B}=\text{Ga, Al}$ ) spinel was proved as new biomarkers due to its persistent luminescence.<sup>10</sup> Therefore, exploration of optical functionalization of cryolite host is meaningful and necessary to create some big opportunities for advanced red/deep red light-emitting diodes (LEDs) and ideal probes for molecular imaging and tissue imaging *in vivo*.

A facile synthesis method of cryolite micron-/nano-crystals should be explored systematically. Mike *et al.* successfully developed an alkoxied sol-gel route for the

complex fluorides of  $\text{MAlF}_4$  ( $\text{M}=\text{K}, \text{Cs}$ ),  $\text{M}_3\text{AlF}_6$  ( $\text{M}=\text{Li}, \text{Na}, \text{K}$ ) and  $\text{Na}_5\text{Al}_3\text{F}_{14}$  (chiolite).<sup>11</sup> However, the reaction obtaining pure phase cryolite went through high temperature at  $\sim 549^\circ\text{C}$  with environmentally unfriendly decomposition. So much energy is required for the synthesis. Also Adachi *et al.* prepared a series of fluoride phosphors,  $\text{A}_2\text{MF}_6:\text{Mn}^{4+}$  ( $\text{A}=\text{K}, \text{Na}, \text{or } \text{NH}_4$ ;  $\text{M}=\text{Si}, \text{Ce}, \text{Zr}, \text{Sn}, \text{or } \text{Ti}$ ) and  $\text{BSiF}_6:\text{Mn}^{4+}$  ( $\text{B}=\text{Ba}, \text{Zn}$ ) by using a lot of HF solution through a wet chemical etching way, which is dangerous for practical operation.<sup>12-17</sup> Hydrothermal reaction has been extensively used to fabricate all kind of inorganic materials with advantages of moderate reaction temperature, controllable reaction process, easy manipulation, more pure products, etc.<sup>18-21</sup> Here we achieved a facile hydrothermal reaction at  $\leq 240^\circ\text{C}$  using different solid fluorine sources to produce large-scale cryolite micron phosphors cheaply. On the other hand, based on the typical thermal decomposition techniques to prepare  $\text{NaYF}_4:\text{RE}^{3+}$ ,  $\text{Yb}^{3+}$  nanocrystals in our lab, we further developed a simple solvothermal decomposition method at moderate temperature using as-prepared trifluoroacetate precursors to synthesize  $\text{Na}_3\text{AlF}_6$ ,  $\text{Na}_3\text{AlF}_6:\text{Cr}^{3+}$  and  $\text{Na}_3\text{AlF}_6:\text{Cr}^{3+}@\text{Na}_3\text{AlF}_6$  NCs in oleylamine solvents.

In this work, we systematically explored the optical functionalization of  $\text{Na}_3\text{AlF}_6$  host by employing  $\text{RE}^{3+}$  ( $\text{RE} = \text{Er}, \text{Eu}, \text{Pr}$ ) and TM ( $\text{TM} = \text{Cr}^{3+}, \text{Ni}^{2+}, \text{Mn}^{2+}, \text{Fe}^{3+}$ ) ions to replace the  $\text{Al}^{3+}$  sites, respectively. It is proved that substitution of  $\text{Al}^{3+}$  site by  $\text{RE}^{3+}$  ions cannot be doped in  $\text{Na}_3\text{AlF}_6$  host lattice even at a little bit around 0.1 mol%  $\text{RE}^{3+}$ , due to large radii mismatch between  $\text{RE}^{3+}$  ( $r \sim 1.10 \text{ \AA}$ , coordination number ( $\text{CN}$ ) = 6) and  $\text{Al}^{3+}$  ( $r = 0.535 \text{ \AA}$ ,  $\text{CN} = 6$ ).<sup>22</sup> As expected, TM ions are successfully doped into  $\text{Na}_3\text{AlF}_6$  lattice by replacing  $\text{Al}^{3+}$  sites because of their similar chemical properties and similar ionic radii. Meanwhile, within the monoclinic “mixed-cation fluoride perovskite” structure of  $\text{Na}_3\text{MF}_6$  ( $\text{M} = \text{Al}, \text{Cr}$ ) cryolite crystals, the corner-sharing octahedral network comprises alternating  $[\text{AlF}_6]^{3-}$  and  $[\text{NaF}_6]^{5-}$  octahedra with  $\text{Na}^+$  ions in interstitial sites (Figure 1).<sup>23</sup> The low symmetry of the  $[\text{AlF}_6]^{3-}$  octahedral site in this structure that would be beneficial for the spin-allowed transitions of  $\text{Cr}^{3+}$ .<sup>24</sup> Optical diffuse reflectance spectra, steady luminescence were measured for optical functionalization of  $\text{Cr}^{3+}$  doped cryolite phosphor. Energy decay dynamics was systematically analyzed on the basis of theoretical model and experimental data. Meanwhile, heat-treated  $\text{Na}_3\text{AlF}_6:\text{Cr}^{3+}$  phosphor,  $\text{Na}_3\text{AlF}_6:60\text{mol}\%\text{Cr}^{3+}$  nanocrystals,

and  $\text{Na}_3\text{AlF}_6:60\text{mol}\%\text{Cr}^{3+}@\text{Na}_3\text{AlF}_6$  (core@shell) were proved to have efficient luminescence properties.

## 2. Experimental Methods

Two different kind of synthesise methods were explored to obtain cryolite particles, the first one is hydrothermal reaction for micron crystals, another is solvothermal decomposition for nanocrystals. Both  $\text{RE}^{3+}$  and TM ions were treated as dopants for cryolite host through hydrothermal reaction. Meanwhile, post-heat treatment was applied on  $\text{Na}_3\text{AlF}_6\text{:Cr}^{3+}$  phosphor obtained via hydrothermal reaction. Furthermore, optimized  $\text{Na}_3\text{AlF}_6\text{:60mol\% Cr}^{3+}$  phosphor and  $\text{Na}_3\text{AlF}_6\text{:60mol\% Cr}^{3+}\text{@Na}_3\text{AlF}_6$  (core@shell) were synthesized via solvothermal decomposition for optimal functionalization.

### 2.1. Chemicals

All the reagents are commercially available. Sodium fluoride ( $\text{NaF}$ , 99%, Alfa Aesar, Haverhill, MA), Ammonium fluoride ( $\text{NH}_4\text{F}$ ,  $\geq 98\%$ , Sigma-Aldrich, St. Louis, MO), Chromium (III) nitrate nonahydrate ( $\text{Cr}(\text{NO}_3)_3 \cdot 9\text{H}_2\text{O}$ , 99%, Sigma-Aldrich, St. Louis, MO), Chromium (III) Chloride ( $\text{CrCl}_3$ , 99.99%, Sigma-Aldrich, St. Louis, MO), Aluminum nitrate nonahydrate ( $\text{Al}(\text{NO}_3)_3 \cdot 9\text{H}_2\text{O}$ ,  $\geq 98\%$ , Sigma-Aldrich, St. Louis, MO), Hydrogen fluoride ( $\text{HF}$ , assay  $\geq 48\%$ , Sigma-Aldrich, St. Louis, MO), Erbium nitrate pentahydrate ( $\text{Er}(\text{NO}_3)_3 \cdot 5\text{H}_2\text{O}$ , 99.9%, Sigma-Aldrich, St. Louis, MO),

Praseodymium (III) nitrate hexahydrate ( $\text{Pr}(\text{NO}_3)_3 \cdot 6\text{H}_2\text{O}$ , 99.9%, Sigma-Aldrich, St. Louis, MO), Europium nitrate pentahydrate ( $\text{Eu}(\text{NO}_3)_3 \cdot 5\text{H}_2\text{O}$ , 99.9%, Sigma-Aldrich, St. Louis, MO), Oleylamine ( $\geq 98\%$ , Sigma-Aldrich, St. Louis, MO), Trifluoroacetic acid ( $\text{CF}_3\text{COOH}$  (TFA), 99%; Alfa Aesa, Haverhill, MA), Sodium trifluoroacetate ( $\text{Na}(\text{CF}_3\text{COO})$  (NaTFA), 98%, Sigma-Aldrich, St. Louis, MO), Aluminum carbonate ( $\text{Al}_2(\text{CO}_3)_3$ , basic, Sigma-Aldrich, St. Louis, MO), Absolute Ethanol (200 proof). All the water solvent used in the experiments is deionized (DI) water ( $18.2\text{M}\Omega$ ).

## 2.2. Hydrothermal synthesis

A series of cryolite samples were synthesized via facile hydrothermal reactions. First, we dissolved all the fluoride source chemicals  $\text{NH}_4\text{F}/\text{HF}$  and  $\text{NaF}$  into DI water ( $\sim 40\text{ ml}$ ) and keep stirring with magnetic bar in a glass beaker. Meanwhile, the metal nitrate solutions were prepared by dissolving  $\text{M}(\text{NO}_3)_3$  ( $\text{M} = \text{Al}, \text{Er}, \text{Eu}, \text{Pr}, \text{Cr}$ ) chemicals into DI water ( $\sim 30\text{ ml}$ ). After vigorous stirring to ensure dissolution, the stock fluoride solution was slowly added into the  $\text{M}(\text{NO}_3)_3$  solution to gradually produce white precipitations, and then kept stirring for 30 minutes. During stirring, 10 ml absolute ethanol was added additionally (Figure 2(a)). Then the resultant white

suspension was transferred into a 125 ml Teflon-lined stainless steel autoclave (Parr Instrument Company, Moline, IL, (Figure 2(b))), filled up to 70% of its capacity. The tightly sealed steel autoclave was held in an oven and maintained at 240 °C for 15h. After being slowly cooled down to room temperature, the filtrated precipitate was centrifuged (Avanti J-26 XP centrifuge, Beckman Coulter, Brea, CA) several times with DI water (3500 rpm, 10 min) to remove any possible ionic remnant, and finally dried at 80 °C for 24 h in ambient atmosphere.

For the preliminary exploration of cryolite synthesis, the molar ratio of  $\text{Na}^+/\text{Al}^{3+}$  in the starting materials was manipulated from 5:3 to 9:3. Another tunable factor for the reaction is the fluoride sources:  $\text{NH}_4\text{F}$  and  $\text{HF}$ , which means either  $\text{NH}_4\text{F}$  or  $\text{HF}$  was used to provide enough  $\text{F}^-$  during synthesis. Following exploration of cryolite host, the  $\text{RE}^{3+}$  ( $\text{RE} = \text{Er}, \text{Eu}, \text{Pr}$ ) and TM ( $\text{TM} = \text{Cr}, \text{Mn}, \text{Fe}, \text{Ni}$ ) ions were doped into cryolite using  $\text{NH}_4\text{F}$  as fluoride source with excess  $\text{NaF}$  relative to the  $\text{Na}^+/\text{Al}^{3+}$  molar ratio ~15:3.



### 2.3. Solvothermal synthesis

For the solvothermal reaction of  $\text{Na}_3\text{AlF}_6$  and  $\text{Na}_3\text{AlF}_6:\text{Cr}^{3+}$  nanocrystals, Aluminate Trifluoroacetate ( $\text{Al}(\text{TFA})_3$ ) and Chromium Trifluoroacetate ( $\text{Cr}(\text{TFA})_3$ ) precursors were first prepared by the following steps:  $\text{Al}_2(\text{CO}_3)_3/\text{CrCl}_3$  powder was dissolved in excess TFA solution to basically trigger  $\text{Al}(\text{TFA})_3/\text{Cr}(\text{TFA})_3$  reaction. To help dissolution, the suspension was sonicated for about 1 hour in a 25 ml glass vial, and dried on hot plate (PC-420D Stirring Hot Plate, Corning Life Science, Edison, NJ) at 75 °C until all the liquid evaporated. Every batch of solvothermal synthesis we aim to get 2.5 mmol  $\text{Na}_3\text{AlF}_6$  or  $\text{Na}_3\text{AlF}_6:\text{Cr}^{3+}$  nanocrystals products. The process is: 1) weigh 2.5 mmol  $\text{Al}(\text{TFA})_3$  powder (note: if to synthesize  $\text{Na}_3\text{AlF}_6:\text{Cr}^{3+}$ , total amount of  $\text{Al}(\text{TFA})_3$  and  $\text{Cr}(\text{TFA})_3$  is 2.5 mmol) and 12.5 mmol  $\text{Na}(\text{CF}_3\text{COO})$  powder (5 times of  $\text{M}(\text{TFA})_3$  mole), and store the chemicals in a 25 ml glass vial; 2) add 5 ml TFA solution in the glass vial to dissolve and mix with sonication and to purify the precursors by evaporation at about 80°C on a hot plate; 3) add 15 ml oleylamine to the glass vial, keep it on the hot plate at 80°C for several hours, then vortex the system for 10 minutes and then keep the glass vial at 80°C. Repeat the third step for several times till all the precursors were well dispersed in oleylamine (clear deep yellow); 4) the stock precursor

solution was transferred to a larger glass bottle (100 ml) with stir bar and additional 45 ml oleylamine, which was then placed on the hotplate stirring for about 24 h to ensure homogeneous dilution.

For each batch synthesis, 20 ml precursor solution was taken out to a three-neck flask with a thermocouple inserted into solution to detect the real reaction temperature (see all set-up in Figure 3). Following argon purging, the solution was heated to 125°C and kept for 1 hour with vigorous magnetic stirring (about 320 rpm) to remove water and oxygen completely. Then the temperature was increased to 240°C and maintained at the given temperature for another 1 hour with slow argon purging (about one bubble per second) to finish reaction (note: for cryolite host nanocrystals exploration, other two samples were synthesized at 280°C and 320°C, respectively). After temperature cools down to about 50°C, the absolute ethanol was added into the three-necked flask to extract products, and then we transferred the mixed solution to a 50 ml centrifuge tube and centrifuged it at 8000 rpm for 10 minutes to collect samples. All of collected products were re-dispersed in absolute ethanol and centrifuged for at least 3 times.

Finally, the cleanly washed sample was dispersed in DI water and then freeze-dried to get the nanocrystals powder for all kinds of characterization.

For the further exploration for core@shell samples, after finishing the 300°C core reaction for 1 hour, the reaction solution was cooled down to 125°C. Then 5 ml additional  $\text{Na}_3\text{AlF}_6$  shell precursor was slowly purged into the solution in 10 min (0.5ml/min), and the solution was kept at 125°C for another half hour. Last, the temperature of the solution was increased to 300°C for one more hour still with slow argon purging. The following washing steps are same as before.

#### **2.4. Post-heat treatment on hydrothermal $\text{Na}_3\text{AlF}_6\text{:Cr}^{3+}$ phosphors**

Furthermore, the as-obtained  $\text{Na}_3\text{AlF}_6\text{:Cr}^{3+}$  phosphor was pressed into a quarter inch diameter pellet using a hydraulic press and then placed in a quartz ampoule which was sealed under vacuum for post-heat treatment without considering the pressure. The ampoule was inserted into a furnace and heated from room temperature to 700 °C (270 °C /h), dwelled at 700 °C for 36 h and cooled to room temperature over 2.5 h. After heating, the ampoule was opened in air and the pellet was removed. The pellet was

ground in an agate mortar and pestled for several minutes to produce powder. The powder was stored with a desiccant after grinding.

## **2.5. Becke line measurement**

First, we placed a small drop of the standard index oil on a glass slide. Meanwhile, we inserted the tip of the needle into the powder sample. Then the powder was transferred to the drop of oil on the slide, and a cover slip was placed over the prepared sample. With the assist of an optical microscope, we observed the Becke Line and its movement as the level of focus moved up and down. The bright Becke Line will move into the sample with higher index as the distance between the sample and microscope objective is increased.<sup>25</sup> We repeated the procedure with several standard oil to estimate the index regions of samples.

## **2.6. Characterization**

Phase identification of all the as-obtained phosphor samples were performed on a Siemens D500 X-ray powder diffractometer (XRD, Bruker AXS Inc., Madison, WI) using Cu K $\alpha$  ( $\lambda= 1.5406\text{\AA}$ ) radiation at 40 kV and 40 mA. XRD patterns were collected with a resolution of 0.018°/step and 2s/step in a  $2\theta$  range of 10°-60°. All the Powder Diffraction File (PDF) can be obtained from software PDF-2

2018(<http://www.icdd.com/products/pdf2.htm>), the mentioned standard cards are  $\text{Na}_3\text{AlF}_6$  (PDF # 25-0772),  $(\text{NH}_4)_2\text{NaAlF}_6$  (PDF # 97-24-9157),  $\text{Na}_5\text{Al}_3\text{F}_{14}$  (PDF # 30-1144),  $\alpha\text{-NaErF}_4$  (PDF # 01-077-2041),  $\beta\text{-NaErF}_4$  (PDF # 00-027-0689),  $\beta\text{-NaEuF}_4$  (PDF # 49-1897),  $\text{PrF}_3$  (PDF # 06-0325) and  $\text{Na}_3\text{CrF}_6$  (PDF # 27-0675). Optical diffuse reflectance spectra (300-1000 nm) of the particles were measured with a Shimadzu UV-3600 spectrophotometer (DRS, Shimadzu Scientific Inst., Somerset, NJ) using  $\text{BaSO}_4$  as standard powder. Scanning electron microscopy (SEM) images of the respective powder samples were taken by means of the Carl Zeiss Sigma field emission SEM (Carl Zeiss, Carl Zeiss SMT Inc., Peabody, MA) using the secondary electron detector and operating at an accelerating voltage of 5.0 kV with a working distance of 8.8 mm. Energy-dispersive X-ray (EDX) spectroscopy area scans of the  $\text{Na}_3\text{AlF}_6:x\%\text{Cr}^{3+}$  powder samples were further performed to determine the elemental composition using an accelerated voltage of 15 kV and a reduced working distance of 8.5 mm for an aperture of 60  $\mu\text{m}$ . The size and morphology of the synthesized nanocrystals were characterized by transmission electron microscopy (TEM) (JEOL2010F Tokyo, Japan) operated at 200 keV. Average particle sizes were estimated from the TEM images by

measuring and analyzing ~200 particles manually. Steady photoluminescence and excitation spectra were determined via single photon counting technique on a FSP920 spectrometer (Edinburgh Instruments, Livingston, UK) equipped with 450 W xenon lamp, TMS300 monochromators, and thermo-electronic cooled Hamamatsu R928P photomultiplier tube (PMT) detector. Time-resolved spectra were measured by time-correlated single photon counting technique on the FSP920 system with pulsed excitation sources of a microsecond  $\mu$ F900 Xe lamp. To eliminate signal noise from excitation sources, long-pass filters of 400, 490, and 695 nm (Thorlabs Inc., Newton, NJ) were appropriately applied in the front of detectors. Fluorescence quantum yield of phosphors was measured on a C9220-03 system (Hamamatsu, Bridgewater, NJ) with a 150 W xenon monochromatic lamp and an integrating sphere. All the XRD results and luminescence spectra were plotted through Origin2018, as well as the decay curve fitting analysis.

### 3. Results and discussion

#### 3.1. Phase identification

##### 3.1.1. Hydrothermal Crystallization

The precursor molar ratio of  $\text{Na}^+/\text{Al}^{3+}$  was varied from 5:3 to 9:3 for the hydrothermal reactions with a  $\text{NH}_4\text{F}$  fluorine source at  $240^\circ\text{C}$  for 15 h. The phase of as-obtained products was examined with XRD, as shown in Figure 4. A portion of diffraction peak well indexed as  $(\text{NH}_4)_2\text{NaAlF}_6$ , and while the remained corresponded to cryolite. At a  $\text{Na}^+/\text{Al}^{3+}$  molar ratio of  $\sim 5:3$ ,  $(\text{NH}_4)_2\text{NaAlF}_6$  was the dominate phase. When the  $\text{Na}^+/\text{Al}^{3+}$  molar ratio was increased to 9:3, the  $\text{Na}_3\text{AlF}_6$  phase became dominant. At  $\text{Na}^+/\text{Al}^{3+}$  molar ratios greater than 9:3, phase-pure cryolite was obtained similar results.

Using similar reaction candidate HF as fluorine source and varying the  $\text{Na}^+/\text{Al}^{3+}$  ratio from 5:3 to 9:3, all the measured XRD traces carefully indexed as cryolite and/or chiolite in Figure 5. At smaller  $\text{Na}^+/\text{Al}^{3+}$  ratios  $\sim 5:3$  and  $\sim 6:3$ , we only got chiolite phase, but once the  $\text{Na}^+/\text{Al}^{3+}$  ratio exceeded 6:3, a  $\text{Na}_3\text{AlF}_6$  appeared and converted to single phase at a  $\text{Na}^+/\text{Al}^{3+}$  ratio of  $\sim 9:3$ .

### 3.1.2. Solvothermal Crystallization

Cryolite was also synthesized by solvothermal decomposition at 240, 280 and 320°C. As comparatively shown in Figure 6, all the measured profiles of as-obtained cryolite nanocrystals were all in good agreement with the typical patterns of cryolite standard. These results reveal that phase-pure cryolite powders were successfully fabricated at low-temperature solvothermal reaction, like 240°C. The broadened XRD peaks shown in Figure 6 indicate that the cryolite particles were either smaller in crystalline size or had less crystallinity than powders prepared using  $\text{NH}_4\text{F}$ .

### 3.1.3. Rare Earth doping

As comparatively shown in Figure 7, all the Na-Al-F composites can be well indexed into cryolite. For lower  $\text{Er}^{3+}$ -doping concentration  $\leq 0.1\text{mol}\%$ , no impure phase can be obviously found, but once  $\text{Er}^{3+}$  concentration beyond 0.1mol%, a secondary phase of  $\alpha\text{-NaErF}_4$  emerged clearly. By increasing  $\text{Er}^{3+}$  concentration, additional  $\beta\text{-NaErF}_4$  phase presented at 0.5mol%  $\text{Er}^{3+}$  (Figure 7). At 10mol%  $\text{Er}^{3+}$ , both  $\alpha\text{-NaErF}_4$  and  $\beta\text{-NaErF}_4$  dominated over the phases in the products. Similarly, two unknown peaks around  $30^\circ$  emerged as 0.1mol%  $\text{Eu}^{3+}$  was doped into cryolite (Figure 7), with increasing  $\text{Eu}^{3+}$  concentration, a secondary phase indexed as  $\beta\text{-NaEuF}_4$  was detected,



which became dominant at 10mol%  $\text{Eu}^{3+}$ . Moreover, in the case of  $\text{Pr}^{3+}$ -doping,  $\text{PrF}_3$  impurities were detected at concentrations as low as 0.1mol%. With increasing  $\text{Pr}^{3+}$  concentration to 10mol%,  $\text{PrF}_3$  was a dominant phase (Figure 7). These results indicated that  $\text{RE}^{3+}$  ions with larger ionic radii (coordination number (CN) = 6;  $\text{Er}^{3+}$  ( $r \sim 0.89 \text{ \AA}$ ),  $\text{Eu}^{3+}$  ( $r \sim 0.947 \text{ \AA}$ ),  $\text{Pr}^{3+}$  ( $r \sim 0.99 \text{ \AA}$ )) cannot substitute for  $\text{Al}^{3+}$  in a  $\text{Na}_3\text{AlF}_6$  host, because  $\text{Al}^{3+}$  has a much smaller ionic radius (CN = 6;  $\text{Al}^{3+}$  ( $r = 0.535 \text{ \AA}$ )).<sup>22</sup> This also showed that cryolite is not a good candidate for RE-based optical materials.

To further reveal the  $\text{RE}^{3+}$ -undoped issue in cryolite host, we employed SEM to image the as-synthesized powders. Figure 8 shows the morphologies of  $\text{Na}_3\text{AlF}_6$  doped with 1mol%  $\text{Er}^{3+}$  (a) and 10mol%  $\text{Er}^{3+}$  (b), that doped with 1mol%  $\text{Pr}^{3+}$  (c) and with 10mol%  $\text{Pr}^{3+}$  (d), and that doped with 1mol%  $\text{Eu}^{3+}$  (e) and 10mol%  $\text{Eu}^{3+}$  (f), respectively. We can see the stone-like cryolite powder with dominant distribution from 0.2  $\mu\text{m}$  to several micrometers. However, we can clearly find the secondary products on the surface of cryolite particles even in the case of lower 1mol%  $\text{RE}^{3+}$  doping, such as the rod-like particles in Figures 8(a) and 8(c), and the plate-like particles in Figure 8(b). These phenomena are in good agreement with the results of XRD in Figure 7,

where the secondary phases of  $\beta$ -/ $\alpha$ -NaErF<sub>4</sub>,  $\beta$ -NaEuF<sub>4</sub> and PrF<sub>3</sub> were clearly detected at attempt to dope 1mol% Er<sup>3+</sup>, 1mol% Eu<sup>3+</sup>, and 1mol% Pr<sup>3+</sup> into cryolite host, respectively. Besides, the morphologies of secondary phases imaged in Figure 8 are really similar to that of REF<sub>3</sub> and/or NaREF<sub>4</sub> reported in some literatures using hydrothermal reaction.<sup>26,27,28</sup> As 10mol% RE<sup>3+</sup> doped cryolite, we can see much more secondary phase particles mixed together with cryolite particles (Figures 8(b), 8(d) and 8(f)). These phenomena further validated that the RE<sup>3+</sup> ions with larger radii cannot substitute the Al<sup>3+</sup> sites in Na<sub>3</sub>AlF<sub>6</sub> host lattice at all.

### 3.1.4. Transition metal doping

While RE ions are large, there are many transition metals (TM = Ni<sup>2+</sup> (r ~ 0.55 Å), Mn<sup>2+</sup> (r ~ 0.67 Å), Fe<sup>3+</sup> (r ~ 0.55 Å), Cr<sup>3+</sup> (r ~ 0.615 Å), CN=6) have similar ionic radius to Al<sup>3+</sup>.<sup>22</sup> Furthermore, in some hosts TM ions can act as activators to generate visible-to-NIR emission. For example, Al<sub>2</sub>O<sub>3</sub>: Cr<sup>3+</sup> laser was indicated to produce coherent deep-red light at 694.3nm.<sup>29</sup> Figure 9(a) shows work done with TM ions doping at concentration 2mol%. By fast scan using photospectrometer, we cannot detect any emission from the Mn<sup>2+</sup>, Ni<sup>2+</sup>, and Fe<sup>3+</sup> doped cryolite samples. Thus Cr<sup>3+</sup> activated

cryolite became the only candidate. Figure 9(b) shows that continuously increasing the  $\text{Cr}^{3+}$  concentration from 0.01 to 1 can be done without any formation of secondary phase. No other diffraction peaks for Al- and Cr-containing impurity phases were detected in any sample. These results indicated that the solid solutions,  $\text{Na}_3\text{Al}_{1-x}\text{Cr}_x\text{F}_6$ , formed.

Crystalline  $\text{Na}_3\text{AlF}_6$  and  $\text{Na}_3\text{CrF}_6$  both have monoclinic structure with same space group of P21/n and space group number of 14 ( $\text{Na}_3\text{AlF}_6$ :  $a = 7.769 \text{ \AA}$ ,  $b = 5.593 \text{ \AA}$ ,  $c = 5.404 \text{ \AA}$  and  $\alpha = \gamma = 90^\circ$ ,  $\beta = 90.18^\circ$ ;  $\text{Na}_3\text{CrF}_6$ :  $a = 5.460 \text{ \AA}$ ,  $b = 5.680 \text{ \AA}$ ,  $c = 7.880 \text{ \AA}$  and  $\alpha = \beta = \gamma = 90^\circ$ ). Besides, the effective ionic radius of  $\text{Al}^{3+}$  ( $r = 0.535 \text{ \AA}$ , CN = 6) is considerably close to that of  $\text{Cr}^{3+}$  ( $r = 0.615 \text{ \AA}$ , CN = 6),<sup>22</sup> as well as no charge compensation needed during substitution. Hence  $\text{Na}_3\text{AlF}_6$  is a perfect host to continuously vary  $\text{Cr}^{3+}$  concentration from a regime where it acts as a dopant to a regime where it likely serves as a constituent. As a direct proof of the solid solution, increasing substitution of  $\text{Al}^{3+}$  (smaller radius) by  $\text{Cr}^{3+}$  (larger radius) from 1% to 100%, the XRD peaks like (011) profile of the as-prepared phosphors smoothly shifted toward smaller angle relative to the peaks of pure  $\text{Na}_3\text{AlF}_6$  and finally matched well with that

of pure  $\text{Na}_3\text{CrF}_6$  (Figure 9(b), Appendix). This phenomenon is consistent with the Vegard's rule,<sup>30</sup> and reveals the successful incorporation of  $\text{Cr}^{3+}$  ions into  $\text{Na}_3\text{AlF}_6$ .

The SEM images provided much more direct information about the size and shape of the as-synthesized  $\text{Cr}^{3+}$  doped cryolite, as well as the effects of post-heat treatment on the size and shape. Figure 10(a) shows the typical SEM image of  $\text{Na}_3\text{AlF}_6:60\text{mol}\%\text{Cr}^{3+}$  synthesized via hydrothermal reaction. The image illustrated the cryolite aggregates basic shape, small polyhedral cryolite with smooth surface tended to grow on the surface of larger one, and the diameter of the crystals was determined between  $\sim 250$  nm and  $\sim 1.25$   $\mu\text{m}$ , respectively. To explore elemental composition as well as its distribution of  $\text{Na}_3\text{AlF}_6:\text{Cr}^{3+}$ , EDX mapping analysis was done for the samples of  $\text{Na}_3\text{AlF}_6:60\text{mol}\%\text{Cr}^{3+}$  in Figure 10(b). The EDX elemental composition was determined by comparing relative peak intensities together with the corresponding sensitivity factors of each element and assuming their total intensities to be 100%. All the elements of Na, Al, F and Cr were detected. EDX results revealed that the phosphors have 26.8 wt.% Na, 50.2 wt.% F, 4.9 wt.% Al, and 18.0 wt% Cr. Accordingly, the mole percentage of Cr and Al was further calculated to be about 66mol% and 34mol%, which

is very close to the stoichiometric composition of 60mol%Cr<sup>3+</sup> and 40mol%Al<sup>3+</sup> in the prepared sample. Although the EDX results cannot accurately quantify the molar ratio of Cr<sup>3+</sup> and Al<sup>3+</sup> in Na<sub>3</sub>AlF<sub>6</sub>, they still suggest that the Cr<sup>3+</sup>-doped Na<sub>3</sub>AlF<sub>6</sub> was successfully synthesized by a facile hydrothermal reaction.

As we know, TEM is a crucial tool to investigate nanoparticles. Figure 11(a-b) exhibits the (a) bright-field and (b) dark-field TEM images of Na<sub>3</sub>AlF<sub>6</sub>:60mol%Cr<sup>3+</sup> synthesized via solvothermal reaction. It can be seen that the monodisperse olivary Na<sub>3</sub>AlF<sub>6</sub>:60mol%Cr<sup>3+</sup> nanocrystals well distributed on the TEM grid, and particle size with length ~18 nm and width ~8 nm can be estimated in general. To get more information about the crystals, SAED was operated to distinguish the phase. As shown in Figure 11(c), the SAED patterns convinced the polycrystalline characterization of as-obtained Na<sub>3</sub>AlF<sub>6</sub>:60mol%Cr<sup>3+</sup> nanocrystals, and were further well indexed into diffraction profiles of Na<sub>3</sub>AlF<sub>6</sub> standard, such as (011), (-211), (012), (022) and (-103).

### 3.2. Refractive index value determined by Becke line measurement

As we mentioned above, the refractive index values of cryolite ( $\sim 1.3385$ ) and chiolite ( $\sim 1.349$ ) is rather attractive because of its matching with refractive index of water ( $\sim 1.3325$ ) and part ranging over the index array of tumor/issues ( $1.33-1.48$ ).<sup>4</sup> As shown in the inset of Figure 6, the suspension of cryolite with smaller radius in DI water does make more transparent system due to the similar refractive index to water. So it is really interesting to enable the solid solution with tunable refractive index to meet with some specific requirement, like bioimaging with very small light scattering loss. This kind of solid solution can be used as luminescent host, and also can be utilized as inert shell materials that are coated on luminescent core nanoparticles. So we observed the Becke line and its movement as the level of focus to confirm the interval of samples cryolite/chiolite and cryolite/ $(\text{NH}_4)_2\text{NaAlF}_6$ .

The measured refractive index ranges of solid solutions are shown in Table 1. We can see that the different ratio of chiolite to cryolite (0 to 1) in the solid solution can tunes the refractive index basically from the index value of pure cryolite ( $1.330\sim 1.335$ ) to that of chiolite ( $1.340\sim 1.345$ ). Besides, it is of great interest that the different composition of cryolite/ $(\text{NH}_4)_2\text{NaAlF}_6$  can induce a higher refractive index to

1.380~1.385, which significantly extend the tunable region of ‘cryolite’-based solid solution system for some possible applications. It is noted that we try our best to make the obtained value adequate enough. In practice, if we would like to get more accurate value, the liquid oil needs special mixing to achieve the best possible match and the refractive index of liquid mixture requires measurement using a refractometer.

### 3.3. Optical diffuse reflectance spectrum

To further confirm the successful incorporation of  $\text{Cr}^{3+}$  into  $\text{Na}_3\text{AlF}_6$  host lattice, optical diffuse reflectance spectrum was recorded. As shown in Figure 12(a), typical absorption bands at about 425 nm and 620 nm can be detected, because of electronic transitions from  $^4\text{A}_2$  ground state to  $^4\text{T}_1(4\text{F})$  and  $^4\text{T}_2(4\text{F})$  intermediate states of  $\text{Cr}^{3+}$ , respectively. These transitions belong to inter-configuration spin-allowed processes that are considerably efficient here upon the light absorption in blue and red regions.<sup>30-</sup>

<sup>33</sup> It is reasonable that the as-obtained  $\text{Na}_3\text{AlF}_6\text{:Cr}^{3+}$  products exhibit green color in naked eye (Figure 12(c)). Meanwhile, the as-obtained  $\text{Na}_3\text{AlF}_6\text{:Cr}^{3+}$  suspension after hydrothermal reaction has homogenously green color (Figure 12(b)), and after complete washing with DI water, the dry powders still feature homogenously green color. These observations suggested that our obtained products are real  $\text{Na}_3\text{Al}_{1-x}\text{Cr}_x\text{F}_6$  ( $0 < x \leq 1$ ) solid solutions. Besides, it is of great interest that the  $\text{Na}_3\text{AlF}_6\text{:Cr}^{3+}$  suspension in DI water looks transparent, which is attributed to a nearly complete match between the refractive index  $\sim 1.3325$  of DI water and that  $\sim 1.3385$  of  $\text{Na}_3\text{AlF}_6$  cryolite crystal at room temperature.<sup>2</sup>



### 3.4. Photoluminescence properties

Since  $\text{RE}^{3+}$  ions are insoluble into cryolite, photoluminescence work only focus on TM doped cryolite. With the exploration of steady luminescence using photospectrometer, we cannot detect any emission from the  $\text{Mn}^{2+}$ ,  $\text{Ni}^{2+}$ , and  $\text{Fe}^{3+}$  doped cryolite samples. Thus  $\text{Cr}^{3+}$  doped cryolite was the only material measured with luminescence spectroscopy.

Figure 13 shows the photon-excitation and emission spectra of  $\text{Na}_3\text{AlF}_6:\text{Cr}^{3+}$  phosphors. By monitoring emission at 720 nm, an excitation spectrum of  $\text{Na}_3\text{AlF}_6:\text{Cr}^{3+}$  phosphors were obtained, as shown in Figure 13(a). The spectra were comprised of two broad excitation bands centered at 420 and 620 nm in visible region. These two excitation peaks are typically attributed to the d-d inner transitions of  $\text{Cr}^{3+}$  from the  $^4\text{A}_2$  ground state to the intermediate states of  $^4\text{T}_1(4\text{F})$  and  $^4\text{T}_2(4\text{F})$ ,<sup>33,34,35</sup> respectively. A UV excitation band  $\sim 282$  nm was also detected which is due to the transition from  $^4\text{A}_2$  to  $^4\text{T}_1(4\text{P})$ . By increasing the  $\text{Cr}^{3+}$  concentration in  $\text{Na}_3\text{AlF}_6$ , the excitation bands did not exhibit any noticeable shift. Photoluminescence spectra in Figure 13(b) all show one single broad peak at about 720 nm when excited with 420 or 580 nm light, owing to the spin-allowed transition of  $^4\text{T}_2(4\text{F}) \rightarrow ^4\text{A}_2$  in the case of  $\text{Cr}^{3+}$  ions located in low crystal

field.<sup>31</sup> This emission band is very broad and spans from 640 to 850 nm with a full width at half maximum of about 95 nm. This peak overlaps well with the action spectra recorded for the stimulation of DNA/RNA synthesis as well as that for the increase of cells adhesion ('active' peaks at about 670, 760 and 825 nm),<sup>36,37</sup> as shown by a green dotted curve in Figure 13(b). However, the spin-forbidden transition of  $^2E \rightarrow ^4A_2$  resulting for narrow zero-phonon line luminescence (*R*-lines) was not observed. It may be because the low crystal field surrounding  $Cr^{3+}$  ions enable the  $^4T_2(4F)$  state to lie lower than  $^2E$  state.<sup>31,38</sup> The symmetric characteristics of the broadband emission  $Cr^{3+}$ -doped  $Na_3AlF_6$  suggest that the bonding environment is uniform with respect to chromium ion coordinative number 6.

To optimize the  $Cr^{3+}$ -doping concentration in  $Na_3AlF_6$ , photoluminescence spectra were recorded using 420 nm excitation (Figure 14). The emission intensity of  $Cr^{3+}: ^4T_2(4F) \rightarrow ^4A_2$  rose to a maximum when the concentration of  $Cr^{3+}$  reaches 60mol%. Beyond that value, the emission intensity decreased due to concentration quenching. Concentration quenching is effected due to energy migration from  $Cr^{3+}$  sub-lattice sites to lattice impurities and defects. High  $Cr^{3+}$ -doping concentrations enable this in

$\text{Na}_3\text{AlF}_6$  because it reduces the  $\text{Cr}^{3+}$ -to- $\text{Cr}^{3+}$  interatomic distance.<sup>39,40</sup> Nonetheless  $\text{Na}_3\text{AlF}_6:60\text{mol}\%\text{Cr}^{3+}$  significantly exhibits a 5-fold increase in brightness when compared to  $\text{Na}_3\text{AlF}_6:1\text{mol}\%\text{Cr}^{3+}$ . By means of optical efficiency measurements, the quantum yield value was  $75 \pm 5\%$  under 420 nm excitation. This is comparable to a quantum yield value  $\sim 68\%$  reported for  $\text{Cr}^{3+}$  doped  $\text{Cs}_2\text{NaAlF}_6$ .<sup>41</sup> The emission peak features a distinct redshift from 715 to 745 nm with the increase of  $\text{Cr}^{3+}$ -doping concentration, which is beneficial for applications such as phototherapy and photomorphogenesis. This redshift results from the perturbation effects of crystal field strength on  $\text{Cr}^{3+}$ :  $^4\text{T}_2(4\text{F})$  spin-allowed state because of the large  $\text{Cr}^{3+}$ -doping concentration in the  $\text{Na}_3\text{AlF}_6$  host. Generally, the crystal field strength ( $Dq$ ) can be formulized as,<sup>42,43</sup>

$$Dq = \frac{1}{6}Ze^2\frac{r^4}{R^5},$$

where  $Z$  is the anion charge or valence,  $e$  is the electron charge,  $r$  is the radius of the  $d$  wavefunction, and  $R$  is the bond length. So the dependence of  $Dq$  on bond length can be generalized as  $Dq \propto 1/R^5$  in a specific host. Doping  $\text{Cr}^{3+}$  ions (radius  $\sim 0.615 \text{ \AA}$ ) into  $\text{Na}_3\text{AlF}_6$  by substituting  $\text{Al}^{3+}$  sites (radius  $\sim 0.535 \text{ \AA}$ ) will lead to a shorter  $R$  of Cr-

F bond, and therefore a stronger  $Dq$  crystal strength. Correspondingly, a stronger crystal strength lowers emission energy leading to emission redshift (the set of Figure 14).

To gain insight into energy transfer process, the decay curve of  $\text{Cr}^{3+}$ :  ${}^4\text{T}_2(4\text{F}) \rightarrow {}^4\text{A}_2$  was recorded as function of  $\text{Cr}^{3+}$  concentration under pulsed light excitation of 420 nm. Figure 15 shows the decay curve of dilute  $\text{Na}_3\text{AlF}_6$ :1mol% $\text{Cr}^{3+}$ , which exhibits single exponential behavior. Higher  $\text{Cr}^{3+}$  concentration display faster decay time (312.9 to 85.2  $\mu\text{s}$ ) which are non-exponential. This is because higher  $\text{Cr}^{3+}$  concentration creates additional energy decay paths, like cross-relaxation, energy migration, and impurity/defect-induced non-radiative transitions. A buildup was observed in the first part of the decay curve to reflect the energy feeding process (see inset of Figure 15). For the decay curve of  $\text{Na}_3\text{AlF}_6$ :1mol% $\text{Cr}^{3+}$ , a rise time ( $t_{\text{rise}}$ ) for peak counts was 134  $\mu\text{s}$ . As the  $\text{Cr}^{3+}$  concentration increases, the  $t_{\text{rise}}$  first decreases to 123  $\mu\text{s}$  at 5mol% $\text{Cr}^{3+}$  then to 114  $\mu\text{s}$  at 10mol% $\text{Cr}^{3+}$ . At dopant concentrations ranging from 10mol% to 60mol%, the  $t_{\text{rise}}$  remains constant at  $\sim 114$   $\mu\text{s}$ , further increase of  $\text{Cr}^{3+}$  concentration to 80mol% $\text{Cr}^{3+}$ , the  $t_{\text{rise}}$  decreases to 110  $\mu\text{s}$ , and finally to 109  $\mu\text{s}$  at 100mol% $\text{Cr}^{3+}$ . Correspondingly, it can be speculated that: i) in  $\text{Na}_3\text{AlF}_6$  activated by  $\leq 2\text{mol}\%\text{Cr}^{3+}$

diluted concentration, interionic distance of  $\text{Cr}^{3+}$ -to- $\text{Cr}^{3+}$  is considerably large, about 22.39 Å, so that the energy of  $\text{Cr}^{3+}$ :  $^4\text{T}_1(4\text{F})$  excited by UV-to-blue light only can be thermally decayed to the lower  $^4\text{T}_2(4\text{F})$  far-red emitting state, therefore featuring long rise time  $\sim 134 \mu\text{s}$ ; ii) by increasing  $\text{Cr}^{3+}$  concentration beyond 5mol% to 10mol%, the  $\text{Cr}^{3+}$ -to- $\text{Cr}^{3+}$  interionic distance becomes small from 16.49 Å to 13.09 Å, and the interaction effect between  $\text{Cr}^{3+}$  ions, such as cross-relaxation processes, occurs efficiently to make the depopulation of  $\text{Cr}^{3+}$ :  $^4\text{T}_1(4\text{F}) \rightarrow ^4\text{T}_2(4\text{F})$  faster, therefore exhibiting reduced rise time to  $\sim 115 \mu\text{s}$ ; iii) with further increase of  $\text{Cr}^{3+}$  concentration from 10mol% to 60mol% ( $\text{Cr}^{3+}$ -to- $\text{Cr}^{3+}$  distance  $\sim 7.20 \text{ Å}$ ), the cross-relaxation effects become saturated because there is a single  $\text{Cr}^{3+}$  fluorescence center in such ‘cryolite’ host, and hence simple cross-relaxation paths exist between the energy levels of  $\text{Cr}^{3+}$   $3d^3$  configuration, therefore yielding consistently incremental emission intensity (Figure 14); iv) as  $\text{Cr}^{3+}$  concentration increases beyond 80mol%, even closer interionic distance of  $\text{Cr}^{3+}$ -to- $\text{Cr}^{3+}$ , shorter than 6.55 Å, enables the excited energy to efficiently migrate over  $\text{Cr}^{3+}$  sub-lattice sites but being finally quenched by the inevitable impurities/defects in  $\text{Na}_3\text{AlF}_6:\text{Cr}^{3+}$  host, hence having decreased rise time  $\sim 110 \mu\text{s}$  (the

inset of Figure 15) and sharply reduced emission intensity (Figure 14). In practice, the monoexponential decay curve can be well fitted to a single exponential function of  $I = A_0 \exp(-t/\tau_0)$ , and the nonexponential one is well fitted to a double exponential function of  $I = A_1 \exp(-t/\tau_1) + A_2 \exp(-t/\tau_2)$ , where  $I$  is luminescence intensity;  $A_0$ ,  $A_1$  and  $A_2$  are constant of fitting parameters, respectively;  $t$  is time;  $\tau_0$  is lifetime for the single-exponential decay curve,  $\tau_1$  and  $\tau_2$  are fast and slow lifetime of exponential components for the nonexponential decay curve, respectively. Using the formula of  $\tau = (A_1\tau_1^2 + A_2\tau_2^2)/(A_1\tau_1 + A_2\tau_2)$ ,<sup>44</sup> the average decay time ( $\tau$ ) of the second-order exponential decay curves can be typically evaluated for  $\text{Na}_3\text{AlF}_6:\text{Cr}^{3+}$  samples. The  $t_{\text{rise}}$  rise time, fitting function, R-squared ( $R^2$ ), fitting parameters, and calculated decay time  $\tau$  are summarized as a function of  $\text{Cr}^{3+}$  concentration in Table 2.

Figure 16(a) comparatively shows the emission spectra of  $\text{Na}_3\text{AlF}_6:60\text{mol}\%\text{Cr}^{3+}$  before and after heat-treatment. These two spectra have same band shape in the same regions, which suggests there is no change in ions coordinating  $\text{Cr}^{3+}$  activators. Meanwhile, Figure 10(c) shows that particle size of heat-treated  $\text{Na}_3\text{AlF}_6:60\text{mol}\%\text{Cr}^{3+}$

phosphor becomes bigger (up to about 2-3  $\mu\text{m}$ ) than that of sample (up to about 1.5  $\mu\text{m}$ ) before heat treatment (Figure 10(a)). EDX result in Figure 10(d) indicates the detection of all elements of Na, Al, Cr and F in cryolite formula, and no other increased impurities are caused by the high temperature heat-treatment process. Again, the mole percentage of 57.9mol%Cr<sup>3+</sup> and 42.1mol%Al<sup>3+</sup> were calculated, which is still close to the stoichiometric composition of 60mol%Cr<sup>3+</sup> and 40mol%Al<sup>3+</sup>. These results indicate that the heat treatment at higher temperature  $\sim 700^\circ\text{C}$  does not change the composition of phosphors. Figure 16(a) did showed the heat-treatment process increases emission intensity of Na<sub>3</sub>AlF<sub>6</sub>:60mol%Cr<sup>3+</sup>. Decay curves of Na<sub>3</sub>AlF<sub>6</sub>:60%Cr<sup>3+</sup> before and after heat treatment are plotted in Figure 16(b), respectively. The average luminescence decay time of heat-treated Na<sub>3</sub>AlF<sub>6</sub>:60mol%Cr<sup>3+</sup> is  $\sim 264\mu\text{s}$ , while the sample without heat-treatment is  $\sim 214\mu\text{s}$  (Table 2). This is because of the decreased concentration of energy quenching centers, such as oxidized surface sides or lattice oxygen introduced by higher 60mol%Cr<sup>3+</sup> dopants. The decreased surface area and improved crystallinity of heat-treated phosphor is well known to always improve phosphor brightness.<sup>45</sup>

Furthermore, we investigated the luminescent properties of  $\text{Na}_3\text{AlF}_6:60\text{mol}\%\text{Cr}^{3+}$  nanocrystals relative to that of large micron  $\text{Na}_3\text{AlF}_6:60\text{mol}\%\text{Cr}^{3+}$ , and the shielding effect via an inert  $\text{Na}_3\text{AlF}_6$  as shell on luminescence of  $\text{Na}_3\text{AlF}_6:60\text{mol}\%\text{Cr}^{3+}$  core nanocrystals. Simple XRD profiles were measured for  $\text{Na}_3\text{AlF}_6:60\text{mol}\%\text{Cr}^{3+}$  nanocrystals and  $\text{Na}_3\text{AlF}_6:60\text{mol}\%\text{Cr}^{3+}@\text{Na}_3\text{AlF}_6$  (core@shell) nanocrystals, which matched well with  $\text{Na}_3\text{AlF}_6$  standard. Under excitation of 420 nm,  $\text{Na}_3\text{AlF}_6:60\text{mol}\%\text{Cr}^{3+}$  nanocrystals efficiently yield broadband deep-red emission at  $740\pm 2$  nm (blue dot line in Figure 17(a)). The maximum intensity of nanocrystals was about 30% of that of micron phosphors (red triangle line in Figure 17(a)). Literature indicated that the shell-coated nanoparticles  $\text{NaYF}_4:\text{Yb}^{3+}\text{Er}^{3+}@\text{NaYF}_4$  can lead to high luminescence upconversion intensity compared to core  $\text{NaYF}_4:\text{Yb}^{3+}\text{Er}^{3+}$  nanoparticles.<sup>46</sup> We explored material like  $\text{Na}_3\text{AlF}_6$  used as shell composition to coat on  $\text{Na}_3\text{AlF}_6:\text{Cr}^{3+}$  core through solvothermal decomposition at 300°C. Under 420 nm excitation, emission intensity of core@shell nanocrystals (green square line in Figure 17(a)) increases relative to that of core nanocrystals, and become  $\geq 50\%$  of emission intensity of  $\text{Na}_3\text{AlF}_6:60\text{mol}\%\text{Cr}^{3+}$  micron phosphors. To give insights on energy decay



of  $\text{Cr}^{3+}$  ions, decay curves of  $\text{Na}_3\text{AlF}_6:60\text{mol}\%\text{Cr}^{3+}$  micron phosphors (red triangle line in Figure 17(b)),  $\text{Na}_3\text{AlF}_6:60\text{mol}\%\text{Cr}^{3+}$  nanocrystals (blue dot line in Figure 17(b)) and  $\text{Na}_3\text{AlF}_6:60\text{mol}\%\text{Cr}^{3+}@\text{Na}_3\text{AlF}_6$  nanocrystals (green square line in Figure 17(a)) were measured under pulsed light excitation at 420 nm. As expected, micron particles have longest lifetime of 213.7  $\mu\text{s}$ , core nanocrystals feature shortest lifetime of 32.0  $\mu\text{s}$  due to large surface area to volume ratio and impurities/defects on the surface, and core@shell nanocrystals characterize medium lifetime of 115.9  $\mu\text{s}$ , which was attributed to the effect of the  $\text{Na}_3\text{AlF}_6$  shell to reduce the concentration of surficial  $\text{Cr}^{3+}$  and various ligands coordinating near surface  $\text{Cr}^{3+}$  species.

## 4. Conclusions

Micron cryolite was obtained through hydrothermal reaction using  $\text{NH}_4\text{F}$  as fluorine source at  $240^\circ\text{C}$ , while the cryolite nanoparticles were synthesized with a solvothermal decomposition at  $300^\circ\text{C}$ . Having a series of micron cryolite particles with varying  $\text{Cr}^{3+}$  doping enabled systematic study of the concentration effects on the NIR optical properties. The optimized  $\text{Na}_3\text{AlF}_6:60\text{mol}\%\text{Cr}^{3+}$  phosphor exhibits the maximum broad deep-red emission intensity at  $\sim 720\text{ nm}$ , due to energy migration from  $\text{Cr}^{3+}$  sub-lattice sites to lattice impurities and defects. Energy decay dynamics was systematically analyzed on the basis of theoretical model and experimental data. Heat-treated at  $700^\circ\text{C}$   $\text{Na}_3\text{AlF}_6:60\text{mol}\%\text{Cr}^{3+}$  micron phosphor exhibited better luminescence create big chance for advanced red/far-red light-emitting diodes (LEDs). The efficient luminescence of  $\text{Na}_3\text{AlF}_6:60\text{mol}\%\text{Cr}^{3+}$  and  $\text{Na}_3\text{AlF}_6:60\text{mol}\%\text{Cr}^{3+}$  @  $\text{Na}_3\text{AlF}_6$  nanoparticles were explored compared to micron  $\text{Na}_3\text{AlF}_6:60\text{mol}\%\text{Cr}^{3+}$ , providing chances for some specific application like bioimaging *in vivo*.

Table 1. The measured refractive index value of the cryolite/chiolite solid solution mixture synthesized by different fluorine sources

Na <sup>+</sup> :Al <sup>3+</sup> ratio	NH <sub>4</sub> F source	HF source
5:3	1.380~1.385	1.340~1.345
6:3	1.360~1.365	1.340~1.345
7:3	1.360~1.365	1.335~1.340
8:3	1.360~1.365	1.335~1.340
9:3	1.360~1.365	1.330~1.335

Table 2. Rise time  $t_{\text{rise}}$  of decay curve, fitting function, R-squared ( $R^2$ ), fitting parameter, and calculated decay time as a function of  $\text{Cr}^{3+}$  concentration in  $\text{Na}_3\text{AlF}_6$  under pulsed light excitation of 420 nm.

$\text{Cr}^{3+}$ (%)	$t_{\text{rise}}$ ( $\mu\text{s}$ )	Fitting function	$R^2$	Component lifetime ( $\mu\text{s}$ )	Fitting parameter	Decay time ( $\mu\text{s}$ )
1	134	$I = A_0 \exp(-t/\tau_0)$	0.9992	-	$A_0 \sim 1.4826$	312.9
5	123	$I = A_1 \exp(-t/\tau_1) + A_2 \exp(-t/\tau_2)$	0.9993	$\tau_1 = 116.7$ $\tau_2 = 329.6$	$A_1 \sim 0.8176$ $A_2 \sim 1.0421$	283.3
10	114	$I = A_1 \exp(-t/\tau_1) + A_2 \exp(-t/\tau_2)$	0.9993	$\tau_1 = 136.1$ $\tau_2 = 333.1$	$A_1 \sim 1.1364$ $A_2 \sim 0.7446$	257.5
20	116	$I = A_1 \exp(-t/\tau_1) + A_2 \exp(-t/\tau_2)$	0.9992	$\tau_1 = 127.2$ $\tau_2 = 349.2$	$A_1 \sim 1.4922$ $A_2 \sim 0.5678$	240.6
40	116	$I = A_1 \exp(-t/\tau_1) + A_2 \exp(-t/\tau_2)$	0.9992	$\tau_1 = 79.5$ $\tau_2 = 320.8$	$A_1 \sim 2.0832$ $A_2 \sim 0.7158$	219.7
60	115	$I = A_1 \exp(-t/\tau_1) + A_2 \exp(-t/\tau_2)$	0.9991	$\tau_1 = 87.7$ $\tau_2 = 342.8$	$A_1 \sim 2.1914$ $A_2 \sim 0.5477$	213.7
80	110	$I = A_1 \exp(-t/\tau_1) + A_2 \exp(-t/\tau_2)$	0.9992	$\tau_1 = 65.7$ $\tau_2 = 304.7$	$A_1 \sim 2.7234$ $A_2 \sim 0.6856$	194.4
100	109	$I = A_1 \exp(-t/\tau_1) + A_2 \exp(-t/\tau_2)$	0.9985	$\tau_1 = 30.1$ $\tau_2 = 267.9$	$A_1 \sim 19.647$ $A_2 \sim 0.6666$	85.2

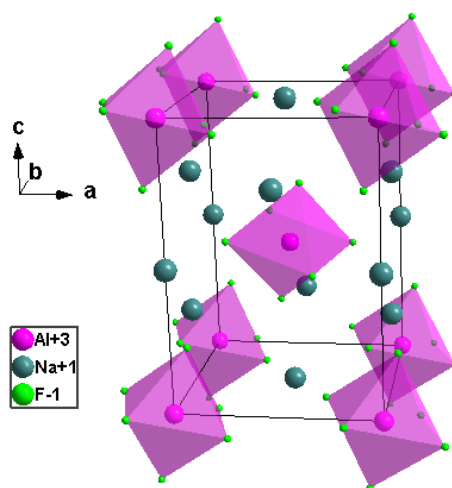


Figure 1 Crystal structures of a typical monoclinic Na<sub>3</sub>AlF<sub>6</sub> cryolite crystal.

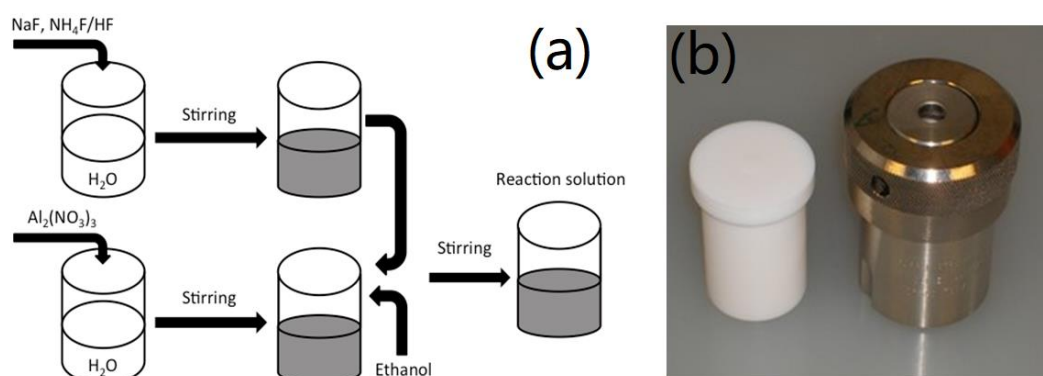


Figure 2 (a) Scheme of facile hydrothermal reaction to synthesize cryolite polycrystals. (b) Optical photograph of Teflon-lined stainless steel autoclave.

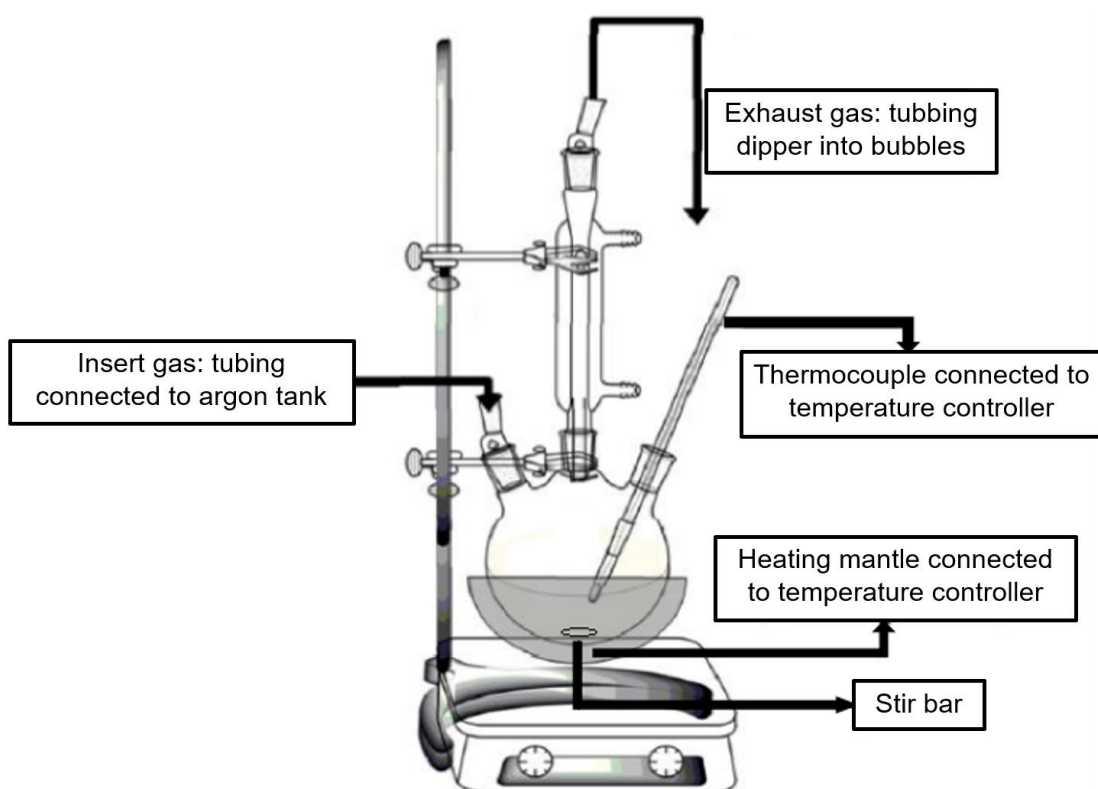


Figure 3 The diagram of solvothermal reaction setup

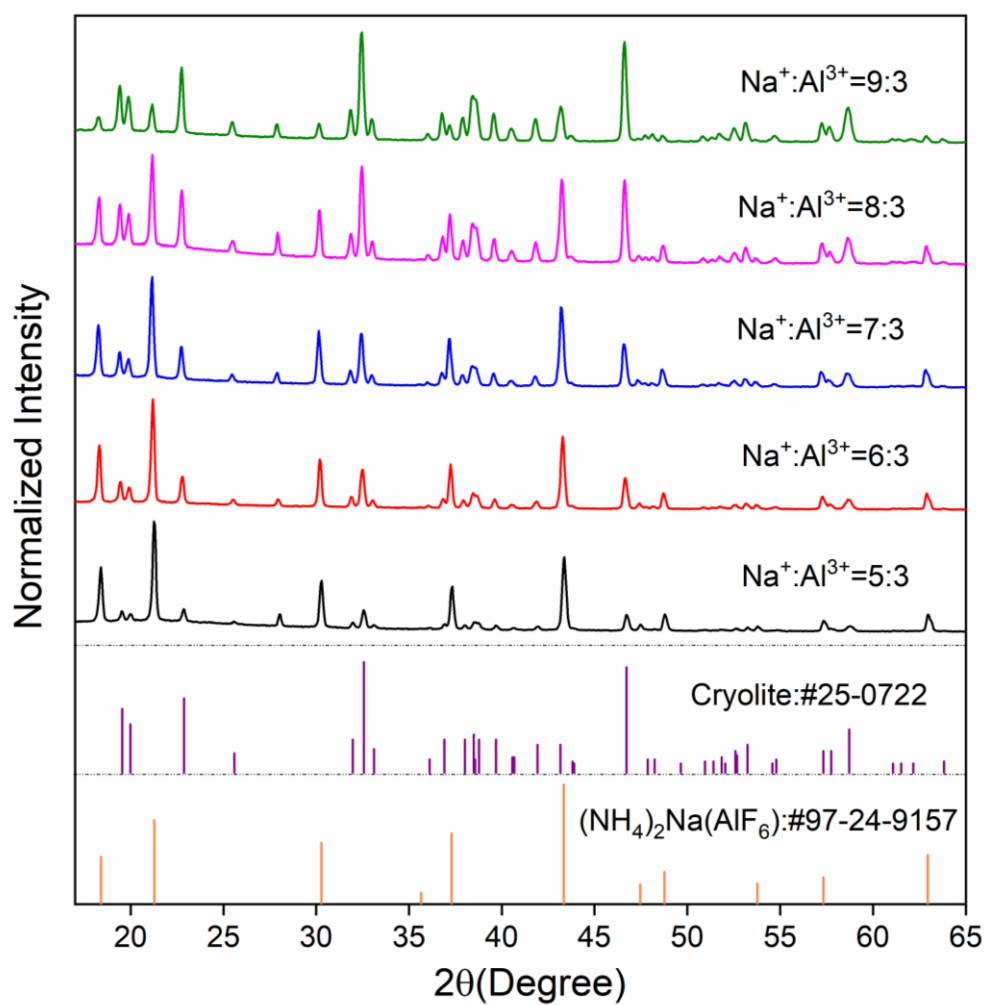


Figure 4 The measured XRD patterns of as-synthesized cryolite powders using  $\text{NH}_4\text{F}$  fluoride source and different ratios of  $\text{Na}^+:\text{Al}^{3+}$  in the raw materials, and the patterns of cryolite (PDF # 25-0772) and  $(\text{NH}_4)_2\text{NaAlF}_6$  (PDF # 97-24-9157) standards.



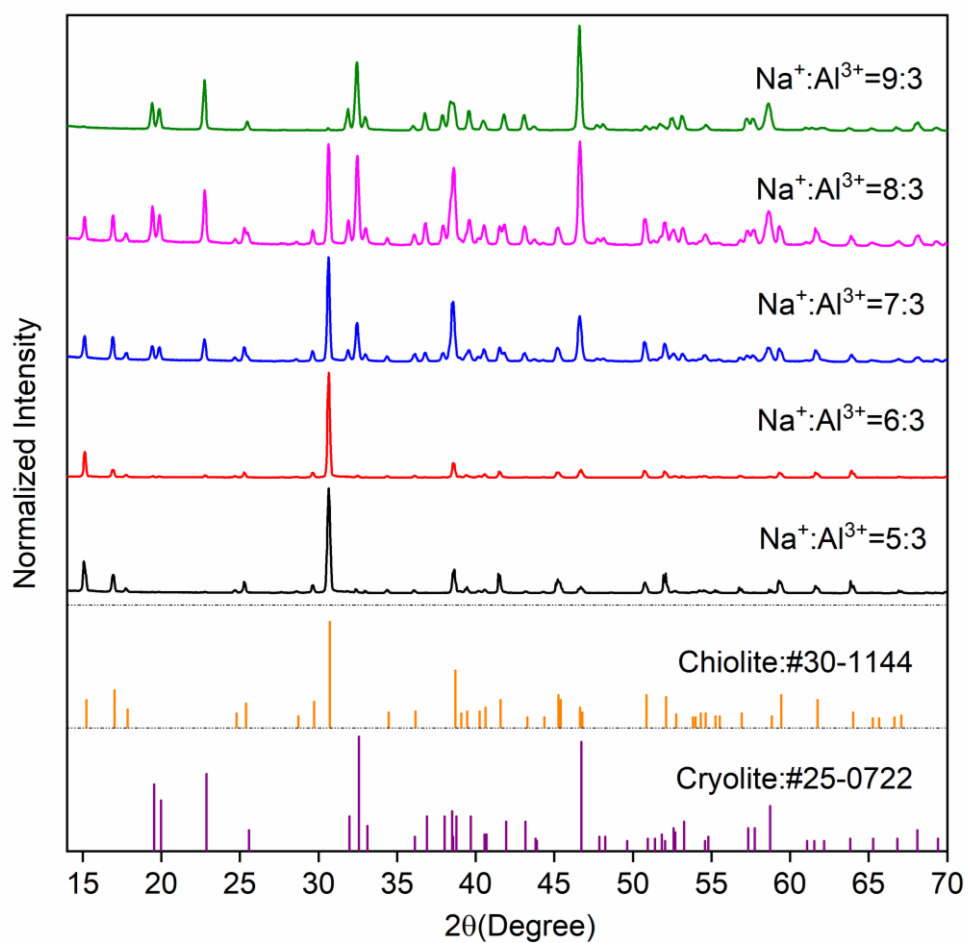


Figure 5 The measured XRD patterns of as-obtained cryolite powders using HF fluoride source and varying Na<sup>+</sup>: Al<sup>3+</sup> ratios in the raw materials, and the patterns of cryolite and chiolite (PDF # 30-1144) standards.

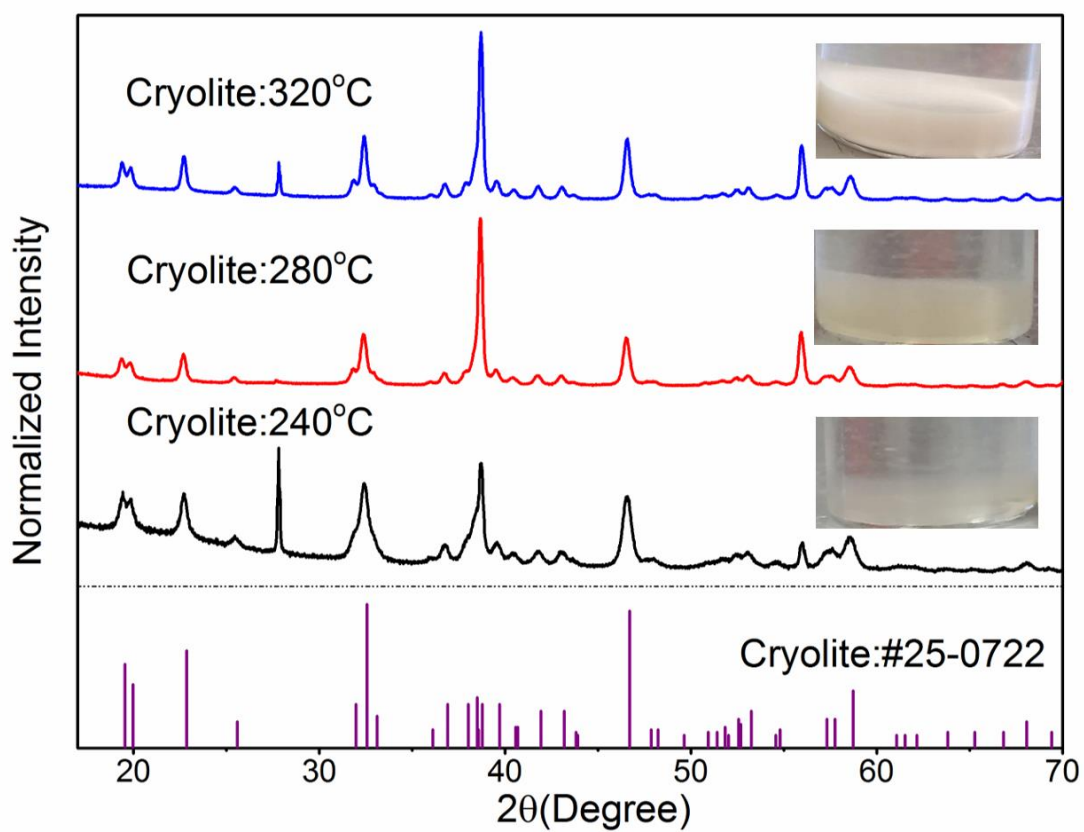


Figure 6 The measured XRD patterns of as-synthesized cryolite nanocrystals at 240, 280 and 320°C, and that of cryolite standard. The image insets show the dispersion of the corresponding cryolite nanocrystals dispersed in DI water.

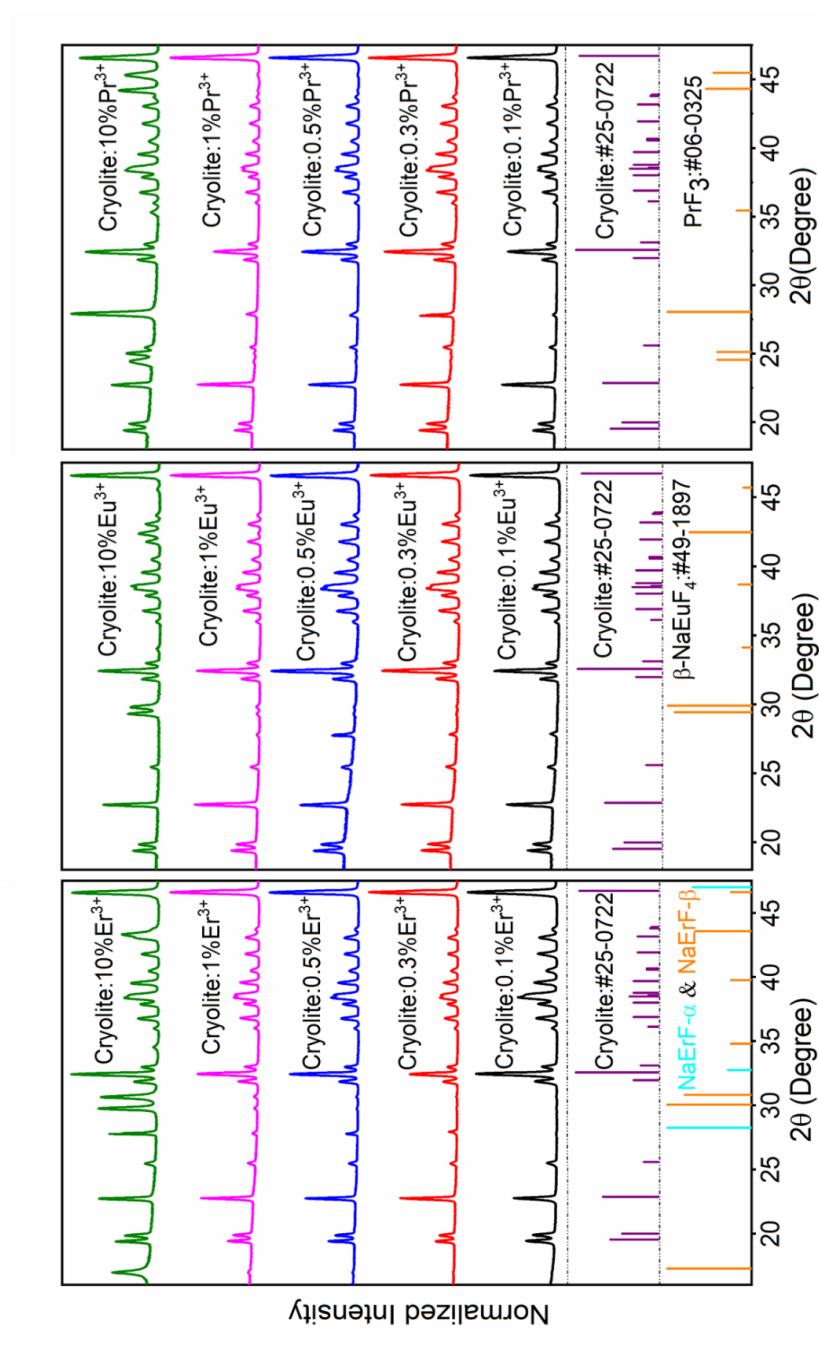


Figure 7 The XRD patterns of the  $\text{RE}^{3+}$ -doped cryolite ( $\text{RE} = \text{Er}, \text{Eu}, \text{Pr}$ ) products and that of cryolite,  $\alpha\text{-NaErF}_4$  (PDF # 01-077-2041),  $\beta\text{-NaErF}_4$  (PDF # 00-027-0689),  $\beta\text{-NaEuF}_4$  (PDF # 49-1897), and  $\text{PrF}_3$  (PDF # 06-0325) standards, respectively.

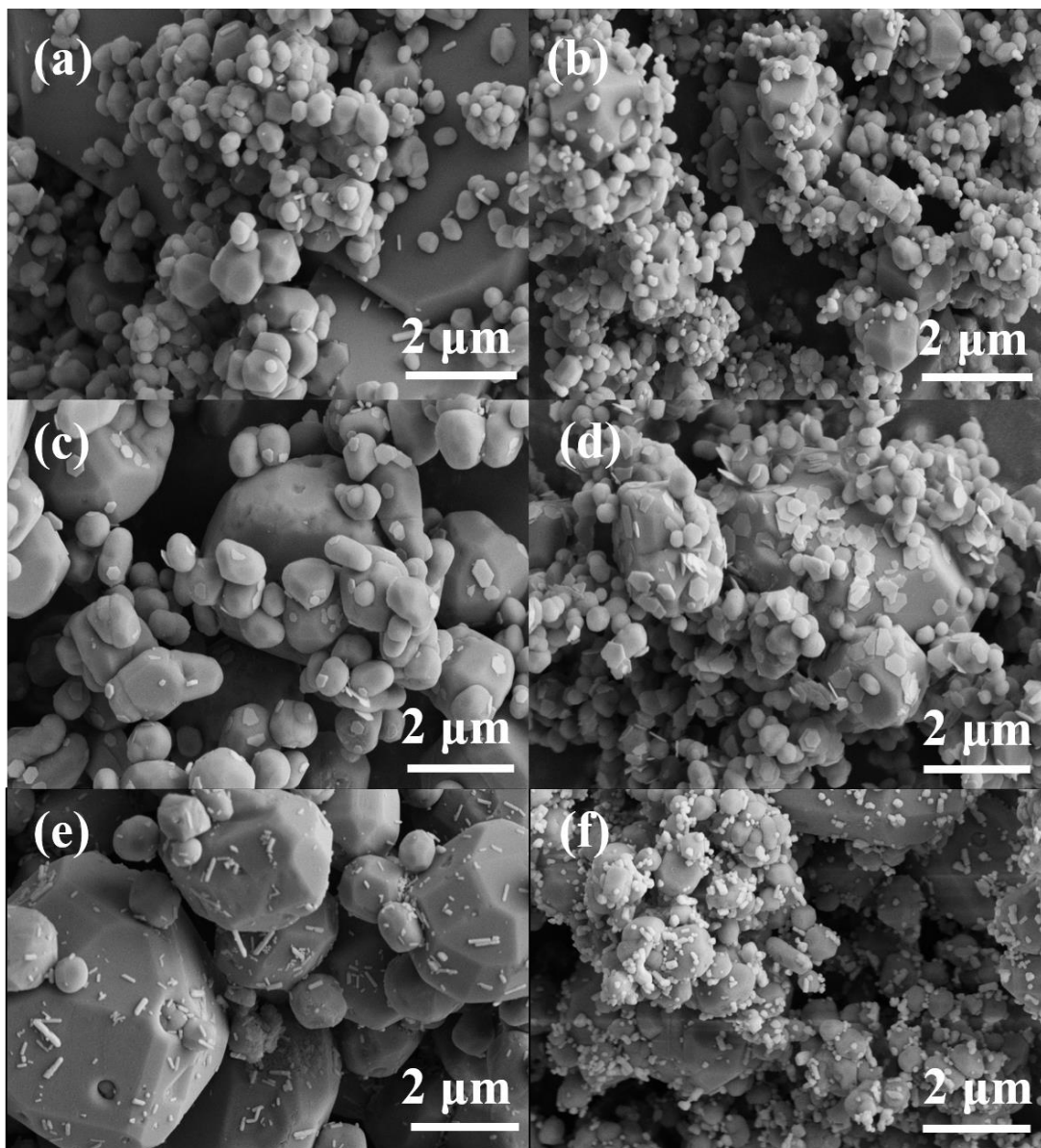


Figure 8 SEM images of  $\text{RE}^{3+}$ -doped cryolite polycrystals synthesized through hydrothermal reaction: (a)  $\text{Na}_3\text{AlF}_6\text{:}1\text{mol\%Er}^{3+}$ , (b)  $\text{Na}_3\text{AlF}_6\text{:}10\text{mol\%Er}^{3+}$ , (c)  $\text{Na}_3\text{AlF}_6\text{:}1\text{mol\%Pr}^{3+}$ , (d)  $\text{Na}_3\text{AlF}_6\text{:}10\text{mol\%Pr}^{3+}$ , (e)  $\text{Na}_3\text{AlF}_6\text{:}1\text{mol\%Eu}^{3+}$ , and (f)  $\text{Na}_3\text{AlF}_6\text{:}10\text{mol\%Eu}^{3+}$ .

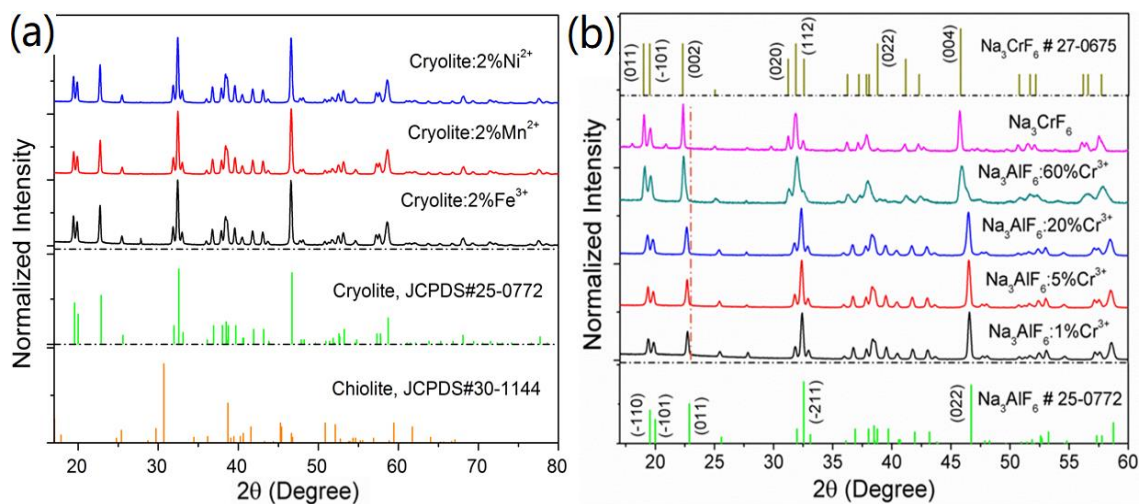


Figure 9 (a) The XRD patterns of hydrothermal synthesized  $\text{Na}_3\text{AlF}_6\cdot 2\text{mol}\%\text{Ni}^{2+}$ ,  $\text{Na}_3\text{AlF}_6\cdot 2\text{mol}\%\text{Mn}^{2+}$ , and  $\text{Na}_3\text{AlF}_6\cdot 2\text{mol}\%\text{Fe}^{3+}$ , and (b) that of  $\text{Na}_3\text{AlF}_6$  doped with various  $\text{Cr}^{3+}$  concentration. The XRD profiles of  $\text{Na}_3\text{AlF}_6$  (PDF # 25-0772),  $\text{Na}_5\text{Al}_3\text{F}_{14}$  (PDF # 30-1144) and  $\text{Na}_3\text{CrF}_6$  (PDF # 27-0675) standards were shown as references

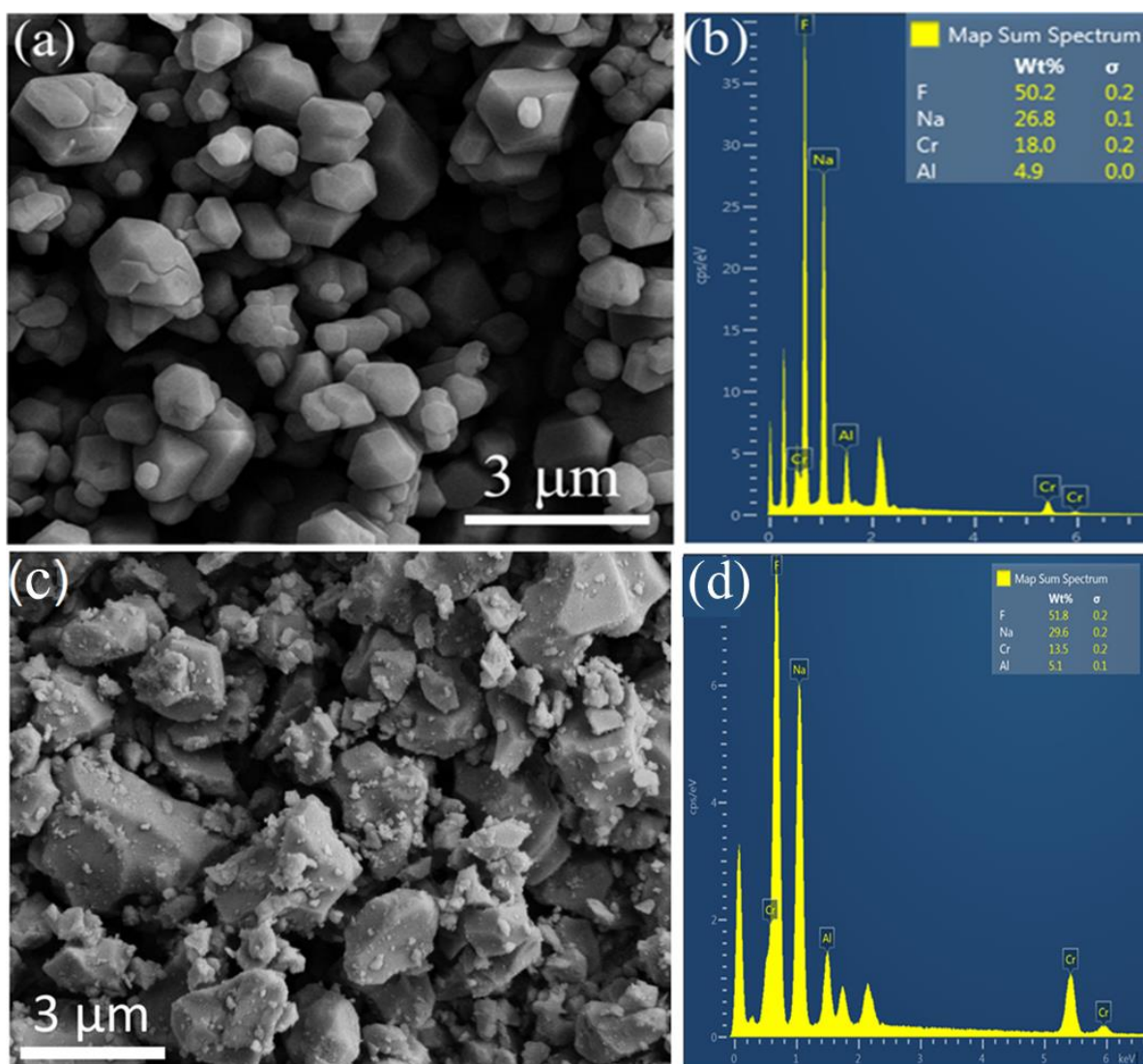


Figure 10 (a) SEM micrograph and (b) EDX spectra analysis of  $\text{Na}_3\text{AlF}_6:60\text{mol}\%\text{Cr}^{3+}$  synthesized via hydrothermal reaction. (c) SEM micrographs and (d) EDX spectra analysis of the corresponding  $\text{Na}_3\text{AlF}_6:60\text{mol}\%\text{Cr}^{3+}$  phosphors heat-treated at 700°C for 36 h.

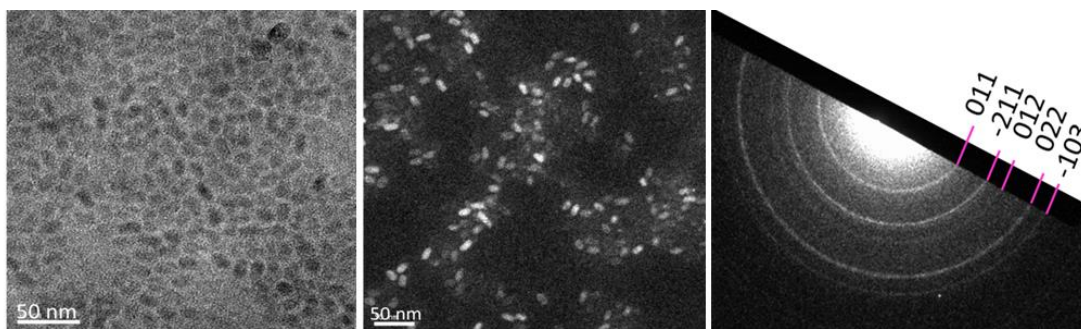


Figure 11 (a) Bright-field and (b) dark-field TEM images and (c) the corresponding SAED patterns of as-synthesized  $\text{Na}_3\text{AlF}_6\text{:}60\text{mol\%Cr}^{3+}$  nanocrystals, respectively.



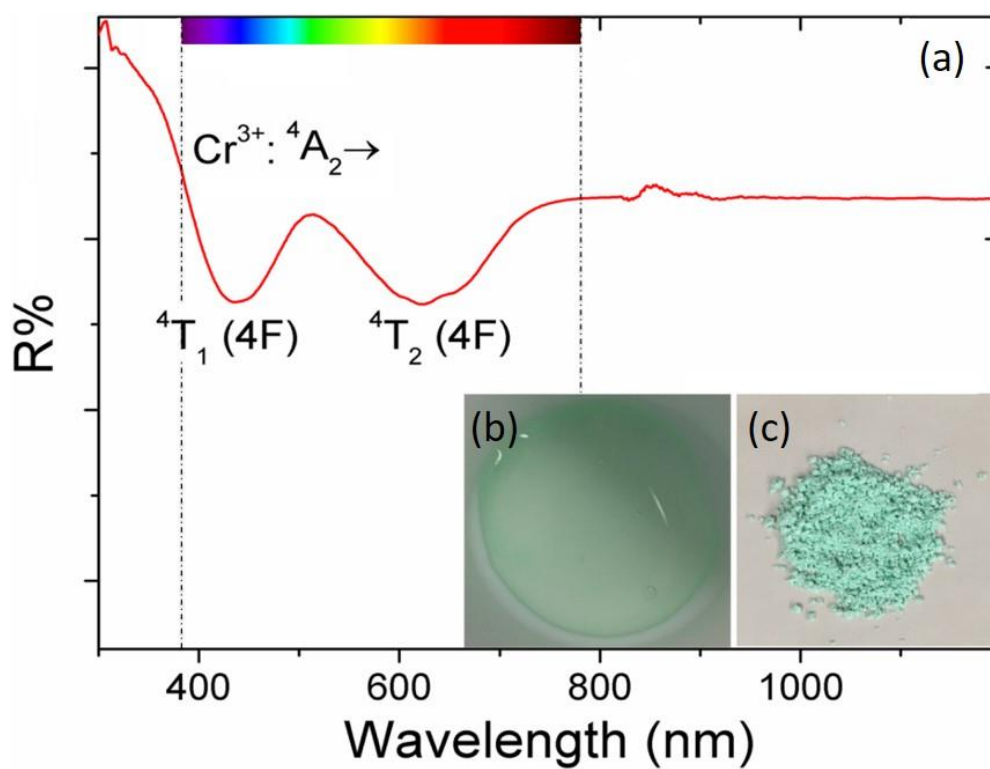


Figure 12 (a) Diffuse reflectance spectrum of  $Na_3AlF_6:Cr^{3+}$  phosphor. (b) The as-obtained  $Na_3AlF_6:Cr^{3+}$  suspension after hydrothermal reaction. (c) The corresponding dry  $Na_3AlF_6:Cr^{3+}$  products after washing. Region confined by dash-dot lines shows wavelength-correlated colorful components to naked eye.



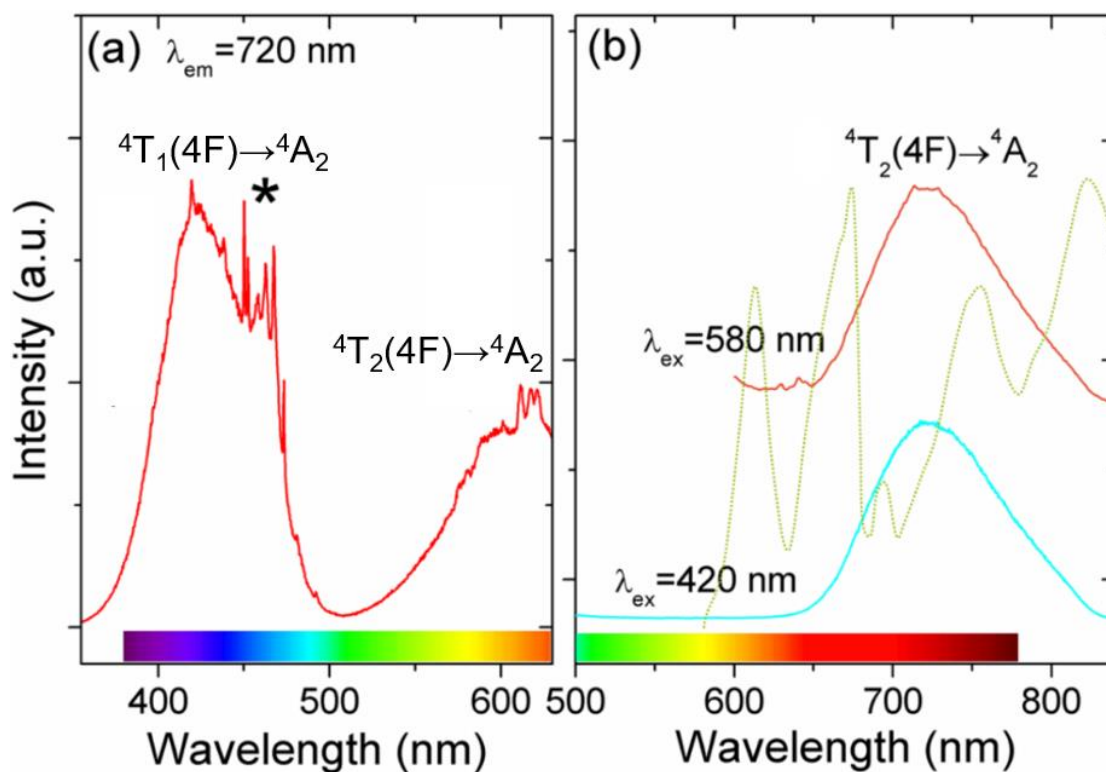


Figure 13 (a) Excitation spectrum of  $\text{Na}_3\text{AlF}_6:\text{Cr}^{3+}$  phosphors monitored at about 720 nm. The black star labels the sharp interference light peaks from xenon lamp around 467 nm. (b) Emission spectra (solid curves) of  $\text{Na}_3\text{AlF}_6:\text{Cr}^{3+}$  under 420 and 580 nm excitation. The bottom colorful bar patterns indicate wavelength-correlated color components to naked eye.

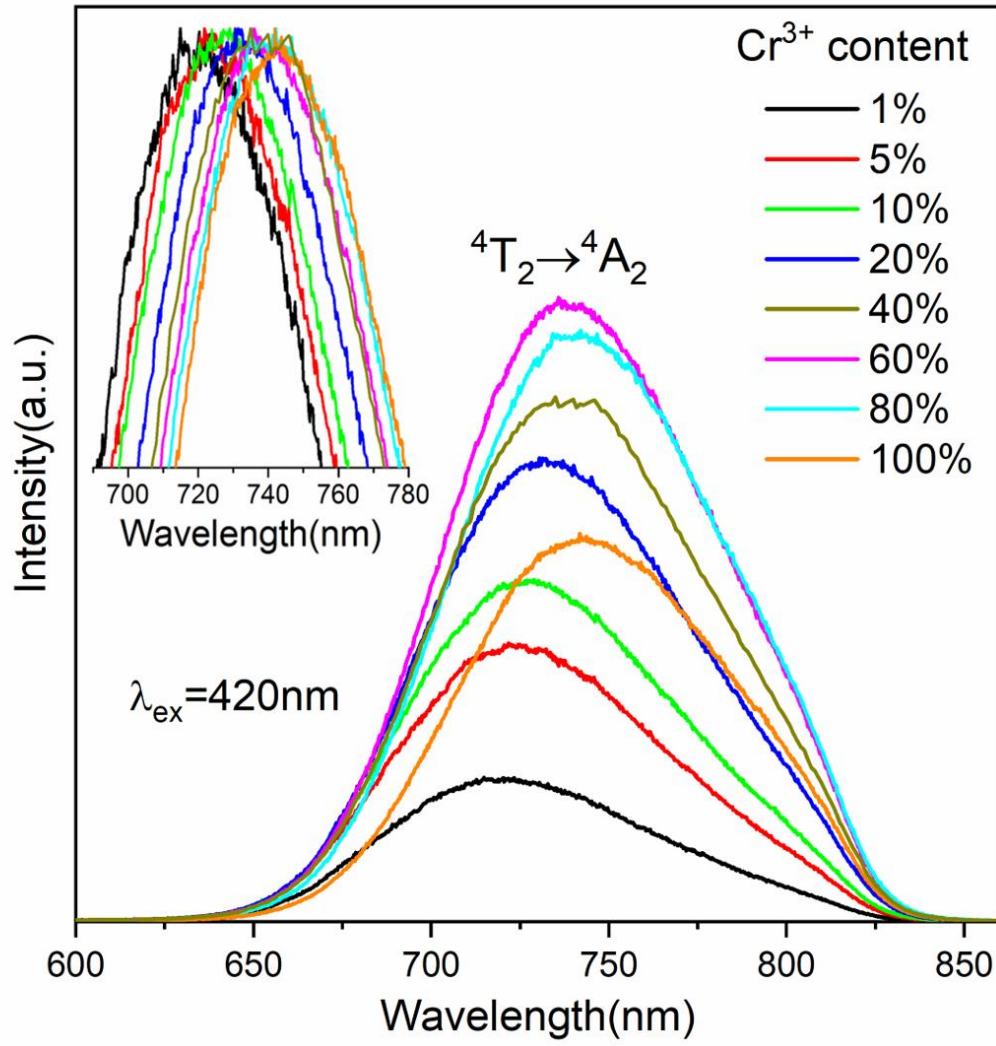


Figure 14 The  $\text{Cr}^{3+}$  concentration-dependent emission spectrum of  $\text{Na}_3\text{AlF}_6:\text{Cr}^{3+}$  phosphors under excitation of 420 nm. Normalized emission intensity in the inset of Figure 14 shows emission peak shift versus  $\text{Cr}^{3+}$  concentration.

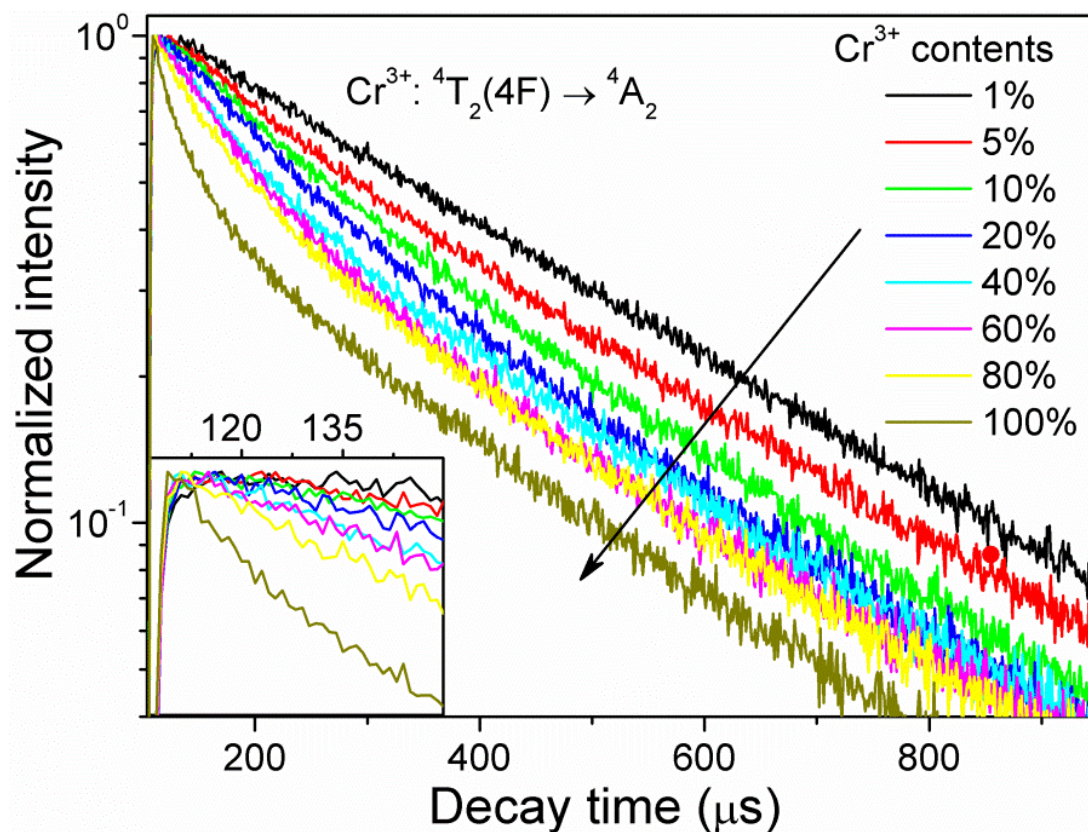


Figure 15 Fluorescence decay curves of  $\text{Cr}^{3+}: {}^4\text{T}_2(4\text{F}) \rightarrow {}^4\text{A}_2 \sim 720 \text{ nm}$  as a function of  $\text{Cr}^{3+}$  concentration in  $\text{Na}_3\text{AlF}_6$  under pulsed light excitation of 420 nm. The inset shows the buildup in the first 150  $\mu\text{s}$  of the curves.

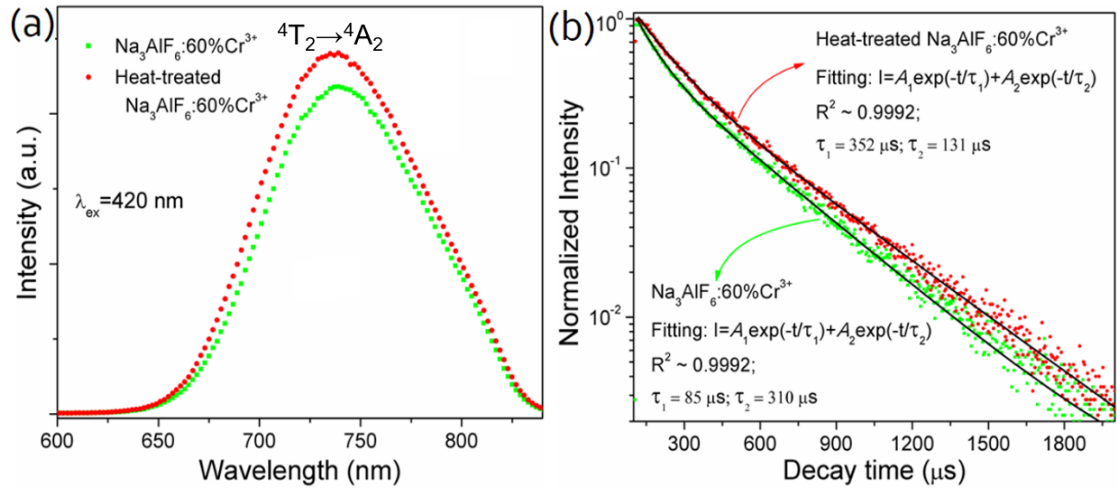


Figure 16 (a) Comparative emission spectra and (b) decay curves of the  $\text{Na}_3\text{AlF}_6:60\text{mol}\%\text{Cr}^{3+}$  sample before (green dot curve) and after (red dot curve) heat treatment, respectively.

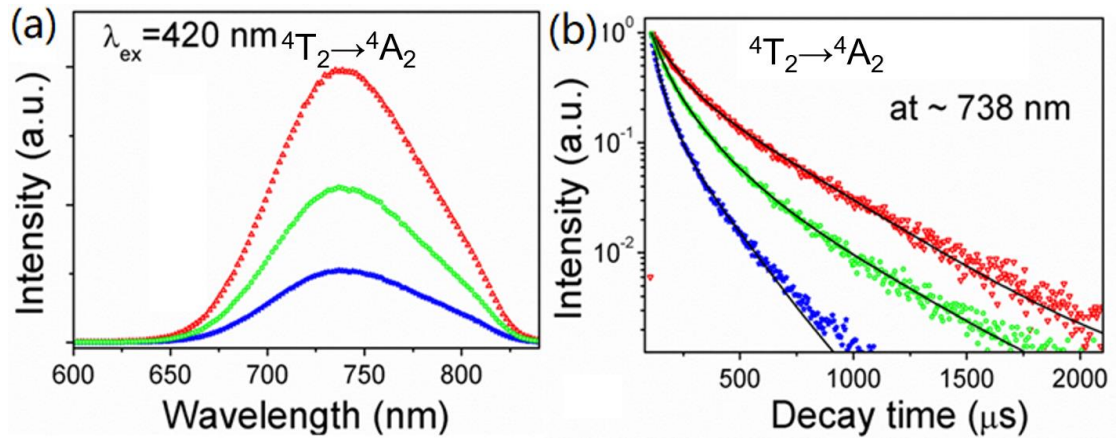


Figure 17 (a) Luminescence spectra and (b) decay curves of  $\text{Na}_3\text{AlF}_6:60\text{mol}\%\text{Cr}^{3+}$  micron phosphors (red triangle line),  $\text{Na}_3\text{AlF}_6:60\text{mol}\%\text{Cr}^{3+}$  nanocrystals (blue dot line) and  $\text{Na}_3\text{AlF}_6:60\text{mol}\%\text{Cr}^{3+}@\text{Na}_3\text{AlF}_6$  nanocrystals (green square line) under excitation of 420 nm, respectively.

## Appendix

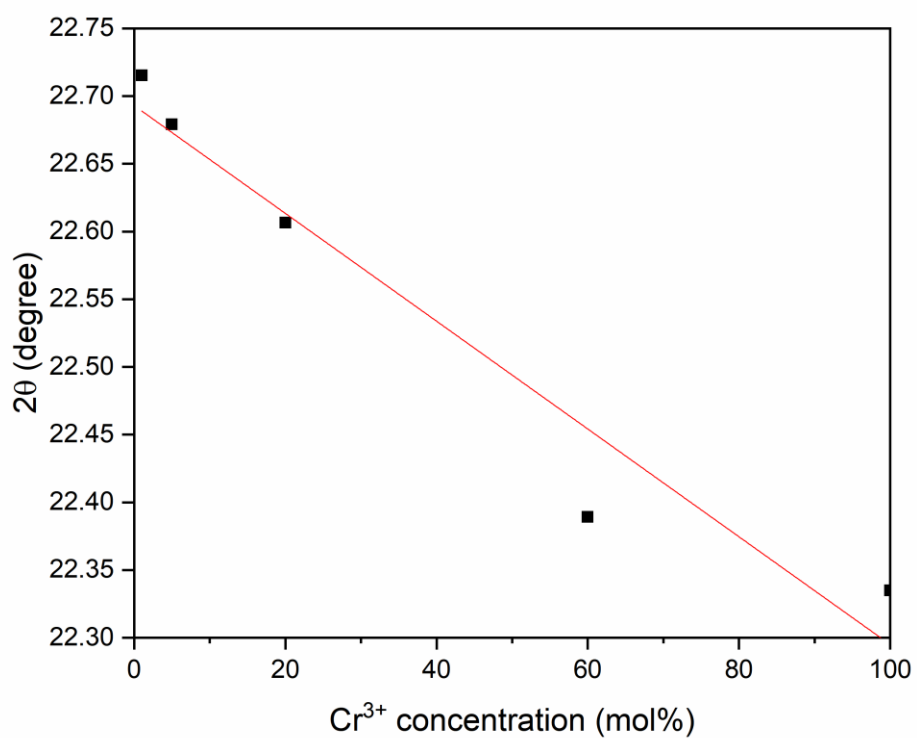


Figure The  $2\theta$  of cryolite peak (011) profile towards  $\text{Cr}^{3+}$  concentration.

## References

- 1) Zhang, Y. S.; Wu, X. X.; Rapp, R. A. Solubility of Alumina in Cryolite Melts: Measurements and Modeling at 1300 K. *Metall. Mater. Trans. B* **2003**, *34* (2), 235-242.
- 2) Cryolite. Website: <https://www.gemdat.org/gem-1161.html>
- 3) Naczynski, D. J.; Tan, M. C.; Riman, R. E.; Moghe, P. V. Rare Earth Nanoprobes for Functional Biomolecular Imaging and Theranostics. *J. Mater. Chem. B* **2014**, *2* (20), 2958-2973.
- 4) Biswas, T.; Luu, T. *In vivo* MR Measurement of Mefractive Index, Relative Water Content and T2 Relaxation Time of Various Bain Lesions with Clinical Application to Discriminate Brain Lesions. *Internet J. Radiol.* **2009**, *13* (1), 1.
- 5) Song, E. H.; Wang, J. Q.; Ye, S.; Jiang, X. F.; Peng, M. Y.; Zhang, Q. Y. Room-temperature synthesis and warm-white LED applications of Mn<sup>4+</sup> ion doped fluoroaluminate red phosphor Na<sub>3</sub>AlF<sub>6</sub>:Mn<sup>4+</sup>. *J. Mater. Chem. C* **2016**, *4*, 2480-2487.
- 6) Liu, Z.; Tabakman, S.; Welsher, K.; Dai, H. J. Carbon Nanotubes in Biology and Medicine: *In vitro* and *In vivo* Detection, Imaging and Drug Delivery. *Nano Res.* **2009**, *2* (2), 85-120.
- 7) Smith, A. M.; Duan, H.; Mohs A. M.; Nie, S. Bioconjugated Quantum Dots for *In Vivo* Molecular and Cellular Imaging. *Adv. Drug Deliv. Rev.* **2008**, *60* (11), 1226-1240.
- 8) Yi, G. S.; Lu, H. C.; Zhao S. Y.; Ge, Y.; Yang, W. J.; Chen, D. P.; Guo, L. H. Synthesis, Characterization, and Biological Application of Size-Controlled Nanocrystalline NaYF<sub>4</sub>:Yb,Er Infrared-to-Visible Up-Conversion Phosphors. *Nano Lett.* **2004**, *4* (11), 2191–2196.
- 9) Wang, L.; Zhang, X.; Hao, Z. D.; Luo, Y. S.; Wang, X.-J.; Zhang, J. H. Enriching Red Emission of Y<sub>3</sub>Al<sub>5</sub>O<sub>12</sub>:Ce<sup>3+</sup> by Codoping Pr<sup>3+</sup> and Cr<sup>3+</sup> for Improving Color Rendering of White LEDs. *Optics Express* **2010**, *18* (24), 25177-25182.
- 10) Sharma, S. K.; Gourier, D.; Viana, B.; Maldiney, T.; Teston, E.; Scherman, D.; Richard, C.; Persistent Luminescence of AB<sub>2</sub>O<sub>4</sub>:Cr<sup>3+</sup> (A = Zn, Mg, B = Ga, Al) Spinel: New Biomarkers for *In Vivo* Imaging. *Opt. Mater.* **2014**, *36* (11), 1901-1906.

- 11) Ahrens, M.; Scholz, G.; Feist, M.; Kemnitz, E. Application of An Alkoxide Sol–Gel Route for the Preparation of Complex Fluorides of the  $MA\text{AlF}_4$  ( $M = \text{K}, \text{Cs}$ ),  $M_3\text{AlF}_6$  ( $M = \text{Li}, \text{Na}, \text{K}$ ), and  $\text{Na}_5\text{Al}_3\text{F}_{14}$  Type. *Solid State Sci.* **2006**, 8 (7), 798–806.
- 12) Xu, Y. K.; Adachi, S. Properties of  $\text{Mn}^{4+}$ -Activated Hexafluorotitanate Phosphors. *J. Electrochem. Soc.* **2011**, 158 (3), J58–J65.
- 13) Kasa, R.; Adachi, S. Red and Deep Red Emissions from Cubic  $\text{K}_2\text{SiF}_6\text{:Mn}^{4+}$  and Hexagonal  $\text{K}_2\text{MnF}_6$  Synthesized in  $\text{HF/KMnO}_4/\text{KHF}_2/\text{Si}$  Solutions. *J. Electrochem. Soc.* **2012**, 159 (4), J89–J95.
- 14) Arai, Y.; Adachi, S. Optical Properties of  $\text{Mn}^{4+}$ -Activated  $\text{Na}_2\text{SnF}_6$  and  $\text{Cs}_2\text{SnF}_6$  Red Phosphors. *J. Lumin.* **2011**, 131 (12), 2652–2660.
- 15) Sekiguchi, D.; Nara, J.-I.; Adachi, S. Photoluminescence and Raman Scattering Spectroscopies of  $\text{BaSiF}_6\text{:Mn}^{4+}$  Red Phosphor. *J. Appl. Phys.* **2013**, 113 (18), 183516.
- 16) Takahashi, T.; Adachi, S. Synthesis of  $\text{K}_2\text{SiF}_6\text{:Mn}^{4+}$  Red Phosphor from Silica Glasses by Wet Chemical Etching in  $\text{HF/KMnO}_4$  Solution. *Electrochem. Solid State Lett.* **2009**, 12 (8), J69–J71.
- 17) Sekiguchi, D.; Adachi, S. Synthesis and Optical Properties of  $\text{BaTiF}_6\text{:Mn}^{4+}$  Red Phosphor. *ECS J. Solid State Sci. Technol.* **2014**, 3 (4), R60–R64.
- 18) Jiang, X. Y.; Pan, Y. X.; Huang, S. M.; Chen, X. A.; Wang, J. G.; Liu, G. K. Hydrothermal Synthesis and Photoluminescence Properties of Red Phosphor  $\text{BaSiF}_6\text{:Mn}^{4+}$  for LED Applications. *J. Mater. Chem. C* **2014**, 2 (13), 2301–2306.
- 19) Li, C. X.; Yang, J.; Quan, Z. W.; Yang, P. P.; Kong, D. Y.; Lin, J. Different Microstructures of  $\beta\text{-NaYF}_4$  Fabricated by Hydrothermal Process: Effects of pH Values and Fluoride Sources. *Chem. Mater.* **2007**, 19 (20), 4933–4942.
- 20) Li, C. X.; Yang, J.; Yang, P. P.; Lian, H. Z.; Lin, J. Hydrothermal Synthesis of Lanthanide Fluorides  $\text{LnF}_3$  ( $\text{Ln} = \text{La to Lu}$ ) Nano-/Microcrystals with Multiform Structures and Morphologies. *Chem. Mater.* **2008**, 20 (13), 4317–4326.
- 21) Li, C. X.; Lin, J. Rare Earth Fluoride Nano-/Microcrystals: Synthesis, Surface Modification and Application. *J. Mater. Chem.* **(2010)**, 20 (33), 6831–6847.
- 22) Shannon, R. D. Revised Effective Ionic Radii and Systematic Studies of Interatomic Distances in Halides and Chalcogenides. *Acta Cryst.* **(1976)**, A32 (5), 751–767.



- 23) Spearing, D. R.; Stebbins, J. F.; Farnan, I. Diffusion and the Dynamics of Displacive Phase Transitions in Cryolite ( $\text{Na}_3\text{AlF}_6$ ) and Chiolite ( $\text{Na}_5\text{Al}_3\text{F}_{14}$ ): Multi-Nuclear NMR Studies. *Phys. Chem. Mineral.* **(1994)**, 21 (6), 373-386.
- 24) Wei, L. L.; Lin, C. C.; Wang, Y. Y.; Fang, M. H.; Jiao, H.; Liu, R. S. Photoluminescent Evolution Induced by Structural Transformation Through Thermal Treating in the Red Narrow-Band Phosphor  $\text{K}_2\text{GeF}_6\text{:Mn}^{4+}$ . *ACS Appl. Mater. Interfaces* **(2015)**, 7 (20), 10656-10659.
- 25) An Introduction to the Methods of Optical Crystallography, by Bloss, F. D. Chapter 5.
- 26) Zeng, S. J.; Ren, G. Z.; Xu, C. F.; Yang, Q. B. High Uniformity and Monodispersity of Sodium Rare-Earth Fluoride Nanocrystals: Controllable Synthesis, Shape Evolution and Optical Properties. *CrystEngComm* **(2011)**, 13 (5), 1384-1390.
- 27) Li, C. X.; Ma, P. A.; Yang, P. P.; Xu, Z. H.; Li, G. G.; Yang, D. M.; Peng, C.; Lin, J. Fine Structural and Morphological Control of Rare Earth Fluorides  $\text{REF}_3$  (RE = La-Lu, Y) Nano/Microcrystals: Microwave-Assisted Ionic Liquid Synthesis, Magnetic and Luminescent Properties. *CrystEngComm* **(2011)**, 13 (3), 1003-1013.
- 28) Tian, Y.; Tian, B. N.; Chen, B. J.; Cui, C. E.; Huang, P.; Wang, L.; Hua, R. N. Morphological Tuning and Enhanced Luminescence of  $\text{NaEuF}_4$  Nano-/Submicro-Crystals. *Appl. Surf. Sci.* **(2014)**, 313 (9), 504-511.
- 29) Van den Hoven, G. N., et al. Upconversion in Er-implanted  $\text{Al}_2\text{O}_3$  waveguides. *Journal of Applied Physics* 79.3 **(1996)**: 1258-1266.
- 30) Yeh, C. W.; Chen, W. T.; Liu, R. S.; Hu, S. F.; Sheu, H. S.; Chen, J. M.; Hintzen, H. T. Origin of Thermal Degradation of  $\text{Sr}_{2-x}\text{Si}_5\text{N}_8\text{:Eu}_x$  Phosphors in Air for Light-Emitting Diodes. *J. Am. Chem. Soc.* **(2012)**, 134 (34), 14108-14117.
- 31) Zhang, Z. Y.; Grattan, K. T.; Palmer, A. W. Temperature Dependences of Fluorescence Lifetimes in  $\text{Cr}^{3+}$ -Doped Insulating Crystals. *Phys. Rev. B* **(1993)**, 48 (11) 7772.
- 32) Yamaga, M.; Macfarlane, P. I.; Henderson, B.; Holliday, K.; Takeuchi, H.; Yosida, T.; Fukui, M. Substitutional Disorder and the Ground State Spectroscopy of Gallogermanate Crystals. *J. Phys.: Condens. Matter* **(1997)**, 9 (2) 569.

- 33) Payne, S. A. Chase, L. L.; Smith, L. K.; Kway, W. L.; Newkirk, H. W. Laser Performance of  $\text{LiSrAlF}_6\text{:Cr}^{3+}$ . *J. Appl. Phys.* **(2002)**, 66 (3), 1051-1056.
- 34) Liu, C. Y.; Xia, Z. G.; Chen, M. Y.; Molokeev, M. S.; Liu, Q. L. Near-Infrared Luminescence and Color Tunable Chromophores Based on  $\text{Cr}^{3+}$ -Doped Mullite-Type  $\text{Bi}_2(\text{Ga,Al})_4\text{O}_9$  Solid Solutions. *Inorg. Chem.* **(2015)**, 54 (4), 1876-1882.
- 35) Chen, D. Q.; Wan, Z. Y.; Zhou, Y.; Zhuo, X. Z.; Yu, Y. L.; Zhong, J. S.; Ding, M. Y.; Ji, Z. G. Dual-Phase Glass Ceramic: Structure, Dual-Modal Luminescence, and Temperature Sensing Behaviors. *ACS Appl. Mater. Interfaces* **(2015)**, 7 (34), 19484-19493.
- 36) Karu, T. I.; Kolyakov, S. F. Exact action spectra for cellular responses relevant to phototherapy. *Photomed. Laser Surg.* **(2005)**, 23, 355–361.
- 37) Sontea, V.; Pocaznoi, I.; Furtuna, D.; Seryakov, A.; Barun, V.; Dick, S. Effects of the low level light therapy on skin wound using LED. In: *IEEE E-Health and Bioengineering Conference* **(2013)**, pp. 1-4.
- 38) Li, Y. J.; Ye, S.; Zhang, Q. Y. Ultra-broadband near-infrared luminescence of ordered-disordered multi-sited  $\text{Cr}^{3+}$  in  $\text{La}_3\text{Ga}_{5.5}\text{Nb}_{0.5}\text{O}_{14}\text{:Cr}^{3+}$ . *J. Mater. Chem. C* 2014, 2, 4636-4641.
- 39) Wegh, R. T.; Donker, H.; Oskam, K. O.; Meijerink, A. Visible Quantum Cutting in  $\text{LiGdF}_4\text{:Eu}^{3+}$  Through Downconversion. *Science* **(1999)**, 283 (5402), 663-666.
- 40) Yu, D. C.; Martín-Rodríguez, R.; Zhang, Q. Y.; Meijerink, A.; Fabouw, F. T. Multi-Photon Quantum Cutting in  $\text{Gd}_2\text{O}_2\text{S:Tm}^{3+}$  to Enhance the Photo-Response of Solar Cells. *Light Sci. Appl.* **(2015)**, 4 (10): e344.
- 41) Torchia, G. A.; Schinca, D.; Khaidukov, N. M.; Tocho, J. O. The luminescent quantum efficiency of  $\text{Cr}^{3+}$  ions in  $\text{Cs}_2\text{NaAlF}_6$  single crystals. *Opt. Mater.* **(2002)**, 20, 301–304.
- 42) Wei, Y.; Qi, X. H.; Xiao, H.; Luo, W. Z.; Yao, H.; Lv, L. F.; Li, G. G.; Lin, J. Site-preferential occupancy induced photoluminescence tuning in  $(\text{Ca,Ba})_5(\text{PO}_4)_3\text{Cl:Eu}^{2+}$  phosphors. *RSC. Adv.* **(2016)**, 6, 43771-43779.
- 43) Dorenbos, P. A review on how lanthanide impurity levels change with chemistry and structure of inorganic compounds. *ECS J. Solid State Sci. Technol.* **(2013)**, 2, R3001-R3011.

- 44) Ma, Y. Y., F. Xiao, S. Ye, and Q. Y. Zhang. Effects of  $\text{Ce}^{3+}$  and  $\text{NH}_4\text{Cl}$  on Structural and Luminescent Properties of  $\text{Y}_2\text{Si}_3\text{O}_3\text{N}_4$ : Ce Phosphors. *Journal of The Electrochemical Society* 159, no. 3, (2012), J39-J42.
- 45) Nakano, Hiromi, Konatsu Kamimoto, Nobuyuki Yokoyama, and Koichiro Fukuda. The Effect of Heat Treatment on the Emission Color of P-Doped  $\text{Ca}_2\text{SiO}_4$  Phosphor. *Materials* 10, no. 9, (2017), 1000
- 46) Wang, Yu, Langping Tu, Junwei Zhao, Yajuan Sun, Xianggui Kong, and Hong Zhang. "Upconversion luminescence of  $\beta\text{-NaYF}_4$ :  $\text{Yb}^{3+}$ ,  $\text{Er}^{3+}$ @  $\beta\text{-NaYF}_4$  core/shell nanoparticles: excitation power density and surface dependence." *The Journal of Physical Chemistry C* 113, no. 17, (2009), 7164-7169.